Monthly Notices
of the
ROYAL ASTRONOMICAL SOCIETY

MNRAS **508,** 245–266 (2021)
Advance Access publication 2021 August 20

https://doi.org/10.1093/mnras/stab2399

The VMC survey – XLIII. The spatially resolved star formation history across the Large Magellanic Cloud

Alessandro Mazzi [1]★ Léo Girardi [2]★ Simone Zaggia [2] Giada Pastorelli [3] Stefano Rubele,[2] Alessandro Bressan,[4] Maria-Rosa L. Cioni [5] Gisella Clementini,[6] Felice Cusano,[6] João Pedro Rocha,[7] Marco Gullieuszik,[2] Leandro Kerber [7] Paola Marigo,[1] Vincenzo Ripepi [8] Kenji Bekki,[9] Cameron P.M. Bell [5] Richard de Grijs,[10,11] Martin A. T. Groenewegen,[12] Valentin D. Ivanov,[13,14] Joana M. Oliveira [15] Ning-Chen Sun[16] and Jacco Th. van Loon[15]

[1]*Dipartimento di Fisica e Astronomia Galileo Galilei, Università di Padova, Vicolo dell'Osservatorio 3, I-35122 Padova, Italy*
[2]*INAF – Osservatorio Astronomico di Padova, Vicolo dell'Osservatorio 5, I-35122 Padova, Italy*
[3]*STScI, 3700 San Martin Drive, Baltimore, MD 21218, USA*
[4]*SISSA, via Bonomea 365, I-34136 Trieste, Italy*
[5]*Leibniz-Institut für Astrophysik Potsdam, An der Sternwarte 16, D-14482 Potsdam, Germany*
[6]*INAF – Osservatorio di Astrofisica e Scienza dello Spazio, Via Gobetti 93/3, I-40129 Bologna, Italy*
[7]*Universidade Estadual de Santa Cruz, Depto. de Ciências Exatas e Tecnológicas Rodovia Jorge Amado km 16, Ilhéus, BA 45662-900, Brazil*
[8]*INAF – Osservatorio Astronomico di Capodimonte, Salita Moiariello 16, I-80131 Naples, Italy*
[9]*ICRAR, M468, The University of Western Australia, 35 Stirling Highway, Crawley, WA 6009, Australia*
[10]*Department of Physics and Astronomy, Macquarie University, Balaclava Road, Sydney, NSW 2109, Australia*
[11]*Research Centre for Astronomy, Astrophysics and Astrophotonics, Macquarie University, Balaclava Road, Sydney, NSW 2109, Australia*
[12]*Koninklijke Sterrenwacht van België, Ringlaan 3, B-1180 Brussels, Belgium*
[13]*European Southern Observatory, Ave. Alonso de Córdova 3107, Vitacura, Santiago 19001, Chile*
[14]*European Southern Observatory, Karl-Schwarzschild-Str 2, D-85748 Garching bei München, Germany*
[15]*Lennard-Jones Laboratories, Keele University, Keele ST5 5BG, UK*
[16]*Department of Physics and Astronomy, University of Sheffield, Hicks Building, Hounsfield Road, Sheffield S3 7RH, UK*

Accepted 2021 August 16. Received 2021 August 16; in original form 2021 April 7

ABSTRACT

We derive the spatially resolved star formation history (SFH) for a 96 deg^2 area across the main body of the Large Magellanic Cloud (LMC), using the near-infrared photometry from the VISTA survey of the Magellanic Clouds (VMC). The data and analyses are characterized by a great degree of homogeneity and a low sensitivity to the interstellar extinction. 756 subregions of size 0.125 deg^2 – corresponding to projected sizes of about 296 × 322 pc^2 in the LMC – are analysed. The resulting SFH maps, with typical resolution of 0.2–0.3 dex in logarithm of age, reveal main features in the LMC disc at different ages: the patchy star formation at recent ages, the concentration of star formation on three spiral arms and on the Bar up to ages of ∼1.6 Gyr, and the wider and smoother distribution of older populations. The period of most intense star formation occurred roughly between 4 and 0.5 Gyr ago, at rates of $\sim 0.3\,M_\odot yr^{-1}$. We compare young and old star formation rates with the observed numbers of RR Lyrae and Cepheids. We also derive a mean extinction and mean distance for every subregion, and the plane that best describes the spatial distribution of the mean distances. Our results cover an area about 50 per cent larger than the classical SFH maps derived from optical data. Main differences with respect to those maps are lower star formation rates at young ages, and a main peak of star formation being identified at ages slightly younger than 1 Gyr.

Key words: galaxies: evolution – Magellanic Clouds – galaxies: structure.

1 INTRODUCTION

Spatially resolved maps of the star formation history (SFH) of nearby galaxies are important essentially for two reasons: first, they help to reconstruct the history of the Local Group, and secondly, they help to improve the current theories of stellar evolution and stellar populations. And, among all nearby galaxies for which spatially resolved SFHs can be derived, the Large Magellanic Cloud (LMC) stands out as a primary target, given its large angular size, proximity (∼50 kpc), and relatively simple geometry. Indeed, the external areas of the LMC can have their SFHs studied using the most simple data and methods available, namely optical ground-based photometry together with colour–magnitude diagram (CMD) reconstruction assuming a mix of stellar populations at a single-distance and low extinction. The inner and more crowded areas, instead, require sharper imaging – which is progressively being expanded with better ground-based surveys and *Hubble Space Telescope* (*HST*) observations – and a proper consideration of dust extinction during the SFH derivation.

★ E-mail: leo.girardi@oapd.inaf.it (LG); alessandro.mazzi@phd.unipd.it (AM)

Descriptions of the past history of the LMC (and the Magellanic System as a whole) include a series of key insights, such as an outside-in quenching of the star formation in fields between 2 and 6 kpc from the LMC centre (Gallart et al. 2008; Meschin et al. 2014), a reduced global star formation taking place until 5–3.5 Gyr ago (Harris & Zaritsky 2009, hereafter HZ09; Weisz et al. 2013), the apparent coupling between field and cluster formation modes (HZ09), and that a common SFH is shared by the LMC Bar and by the inner LMC disc over time-scales of Gyr (Monteagudo et al. 2018). The addition of accurate proper motions (Kallivayalil et al. 2013; Gaia Collaboration 2021b) is creating substantial challenges for the interpretation of these SFHs, but, on the other hand, it is opening the possibility of detailed comparisons between the SFHs of model galaxies derived from cosmological simulations (e.g. Williamson & Martel 2021), and those actually observed in the Magellanic Clouds.

Spatially resolved SFHs are also starting to become an important ingredient to test and improve the theories of stellar evolution and stellar populations. The simplest application of this kind stands on the delay-time distribution (DTD) technique, which relates the counts of a given class of objects with the SFHs of the galaxy region where they are observed. When many different galaxy regions are available, delay-times between the star formation events and the appearance of the objects can be derived, and inform about their lifetimes and progenitor masses. DTDs have so far been applied in the LMC to probe the progenitors of supernova remnants (Maoz & Badenes 2010), planetary nebulae (Badenes, Maoz & Ciardullo 2015), and even RR Lyrae (Sarbadhicary et al. 2021). Another technique relies on the fact that some classes of objects derive from a wide range of stellar masses, whose relative contributions can only be assessed if we have spatially resolved SFHs; comparisons between the numbers modelled and those observed in regions of different mean metallicity and different mean age then inform us on the correctness of model lifetimes, and suggest directions for their improvement. This method requires that the SFH derivation is not affected by the stars whose models are being checked. Examples of this method applied to calibrate evolutionary models of TP-AGB stars in the Magellanic Clouds are given in Pastorelli et al. (2019, 2020).

The results of all these methods depend on the accuracy, reliability, and spatial extension of the derived SFHs. For the main body of the LMC, the classical space-resolved SFH map comes from HZ09, and was derived from ∼64 deg^2 of optical photometry from the Magellanic Clouds Photometric Survey (MCPS; Zaritsky et al. 2004). Different surveys are now aiming to improve these maps by using either deeper optical data, such as the Survey of the MAgellanic Stellar History (SMASH; Nidever et al. 2017, 2021), or the near-infrared data, such as the VISTA[1] survey of the Magellanic Clouds (VMC; Cioni et al. 2011).

Last but not least, the LMC is, traditionally, a main anchor in the measurement of the Hubble constant (H_0) through the cosmic distance ladder. A consistent and homogeneous SFH derived over the whole body of the LMC is crucial to disentangle how the LMC morphology impacts distances measured using most important and widely used standard candles such as Cepheids, RR Lyrae, and eclipsing binaries.

In this paper, we derive the space-resolved SFH across the disc of the LMC using 63 tiles of VMC data for a total area of 96 deg^2. This work supersedes the preliminary results presented in Rubele et al. (2012) and Pastorelli et al. (2020) for smaller subsets of the VMC data for the LMC (regarding 4 and 11 tiles, respectively), and complements the analyses of the SFH for the Small Magellanic Cloud (SMC) using the same survey (Rubele et al. 2015, 2018). A distinctive characteristic of the present analysis is the great uniformity of the entire data set, which we match with a uniform method of analysis. In addition, the use of near-infrared data ensures a reduced sensitivity of the results on the extinction, both internal and external to the LMC.

This paper is structured as follows: Section 2 presents the VMC data and its processing for the aims of this paper. Section 3 describes the method we adopt to derive the SFH together with examples for a couple of LMC subregions. Section 4 presents the results for the large-scale map of the SFH, and the distances and extinctions we derive as a by-product of the method. Section 5 presents some additional analyses, namely a first-order description of the LMC geometry based on the distance map and a comparison of the SFH map with the HZ09 one. Section 6 summarizes the main results.

2 THE VMC DATA

2.1 Selected tiles and PSF photometry

From 2009 to 2018, the LMC was observed in the filters Y, J, and K_s of the VISTA Infra Red CAMera (VIRCAM; Dalton et al. 2010), as part of the VMC survey. For this work, we select 63 LMC tiles covering a total area of ∼96 deg^2. Their distribution on the sky is plotted in Fig. 1. The larger tile dimension is aligned close to the north–south direction.

For all these tiles, we retrieve the pawprint data from the VISTA Science Archive (Cross et al. 2012). Image stacking and point spread function (PSF) photometry are performed as described in Rubele et al. (2015, 2018), using the VISTA photometric zero-points v1.3 (González-Fernández et al. 2018, see also Section 4.3 below). In the following text, we just consider the 'almost-uniformly covered' section of each tile, i.e. the parts covered at least twice in the tiling of six pawprints, with an area of 1.017° × 1.475° (out of a total 1.201° × 1.475° area observed on the sky). This selection ensures more uniform photometry at a modest cost in terms of total covered area.

The photometric catalogues are then split into 12 subregions per tile for the subsequent SFH analysis. As in Rubele et al. (2012), the subregions are numbered from G1 to G12, as illustrated in the left-hand panel of Fig. 1. For the sake of brevity, we adopt the following convention in this paper: subregions are referred to as Tt_Gg, where t is an abbreviated number of the LMC tile from VMC, and g is the subregion number from 1 to 12. For instance, according to this scheme the subregion G5 of the tile LMC 3_2 becomes T32_G5.

The left-hand panel of Fig. 1 illustrates the number of stars available per subregion. Some details worth of mention are:

(i) There is a 30 per cent decrease in the numbers of stars observed in the subregions G9, in the south-western corner of each tile. This is due to a cut we do in the photometric catalogues, to eliminate the area covered by the top-half of the VIRCAM detector 16, which presents a variable quantum efficiency and hence unreliable photometry (see section 6.1 of Cross et al. 2012).[2]

[1]VISTA is the Visible and InfraRed Survey Telescope for Astronomy (Emerson, McPherson & Sutherland 2006), a 4-m telescope located at the Cerro Paranal site of the European Southern Observatory (ESO).

[2]From the 12 600 × 15 500 pixels of the stacked LMC tiles, the two areas cut from G9 correspond to the intervals with $x = [9700, 12\,600]$, for $y = [0, 800]$ and $y = [1870, 2740]$.

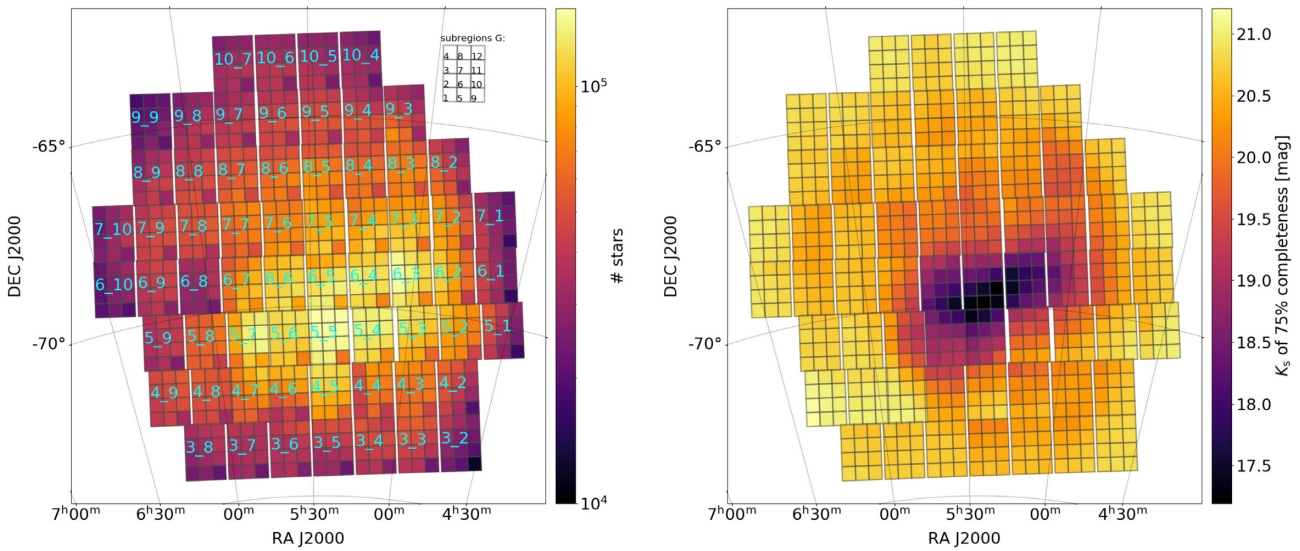

Figure 1. The left-hand panel shows a map of the VMC tiles and subregions considered in this work. Tiles are labelled in cyan, and the inset at the top-right illustrates the numbering of the subregions from G1 to G12, which applies to all tiles. The colour scale indicates the total number of stars detected in both J and K_s for each subregion, hence revealing the large scale-structure of the LMC disc and its bar. A few tiles have reduced star counts compared to their neighbours, owing to their particular observing conditions (e.g. a worst than usual seeing, the presence of thin cirrus, etc.). The reduced stellar numbers in all subregions G9 are due to the masking we perform to avoid the defective area of VIRCAM detector 16. The right-hand panel shows the same map with a colour scale indicating the K_s magnitude at which the completeness falls below 75 per cent, for stars with $J-K_s = 0$. These maps are obtained from the J and K_s photometry, but very similar maps are obtained for the Y and K_s photometry.

(ii) Also evident are narrow vertical gaps between adjacent tiles – regions discarded because observed just once in the tiling of six pawprints.

(iii) The subregions correspond to projected sizes of about 296 × 322 pc^2 (in the east–west × north–south directions) at the LMC distance of ∼50 kpc.

We remark that the total area observed by the VMC survey across the LMC comprises 68 tiles. In this work, we use only 63 because for the others, located in the southern part of the LMC, the processing has not yet reached the same level of homogeneity.

In Fig. 2, we present examples of CMD derived from these data, for (1) subregion T32_G5, which is a peripheral, low-density region without signs of star formation younger than ∼1 Gyr, and (2) T86_G5, located over the extended Constellation III in the northern part of the LMC disc, which presents clear signs of recent star formation and a larger stellar density. In the case of T32_G5, the CMDs present the features expected from intermediate-age and old populations (with ages between 1 and 12.7 Gyr) at the distance of the LMC, in particular the main sequence (MS) at $K_s > 19$ mag, the red clump (RC) at $K_s \simeq 17$ mag, and the extended red giant branch (RGB) stretching diagonally; moreover, the Milky Way (MW) foreground defines two almost-vertical stripes in the CMDs: a prominent one at $K_s > 14$ mag at colours $Y - K_s \simeq 1.3$ mag and $J - K_s \simeq 0.8$ mag, and a less marked one for all K_s and colours $Y - K_s \simeq 0.7$ mag and $J - K_s \simeq 0.4$ mag. In the case of T86_G5, additional features coming from young populations become prominent, including an MS extending upwards to $K_s \simeq 14$ mag, and the presence of bright core-helium burning stars among the MW features (especially at $K_s \simeq 14$ mag, in this case).

Regions T32_G5 and T86_G5 represent most of the range of stellar densities found in the survey: indeed when we rank all subregions by their density of bright ($K_s < 18$ mag) and uncrowded stars, T32_G5 and T86_G5 are at the second and 71th percentiles of the distribution, respectively. They do not represent the high-density tail of the distribution, which will be discussed later starting from Section 4.1. Also, we note that even the lowest dense subregion presents clear LMC features in its CMD, just like in the case of T32_G5. There are no fields dominated by foreground stars and background galaxies, which could be used as a template to remove the LMC foreground/background.

2.2 Preparing the initial Hess diagrams

The SFH analysis essentially consists of reproducing the numbers of stars in many bins across the CMDs. To do that, we start by converting the data into Hess diagrams, which are matrix representations of the stellar density across the CMD, using regularly spaced colour–magnitude bins. We define Hess diagrams with the following characteristics:

(i) From the YK_s photometry, we define 275 × 70 bins, for K_s between 11 and 22 mag with a 0.04 mag width, and for $Y-K_s$ between −0.8 and 2 mag with 0.04 mag width;

(ii) From the JK_s photometry, we define 275 × 50 bins, with the same limits and spacing for K_s, and for $J-K_s$ between −0.5 and 1.5 mag with 0.04 mag width.

These limits are wide enough to include the bulk of stars in the observed CMDs (see Fig. 2). The size of the colour–magnitude bins represent a pragmatic choice that will ensure both a good convergence of the SFH-recovery tools (because of the large star counts across the MS, RC, and RGB, at least), and a good sensitivity to some astrophysically interesting quantities such as the distance modulus, mean extinction, and metallicity (Section 4). Hereafter, we will refer to these two kinds of Hess diagrams as the JK_s and YK_s cases.

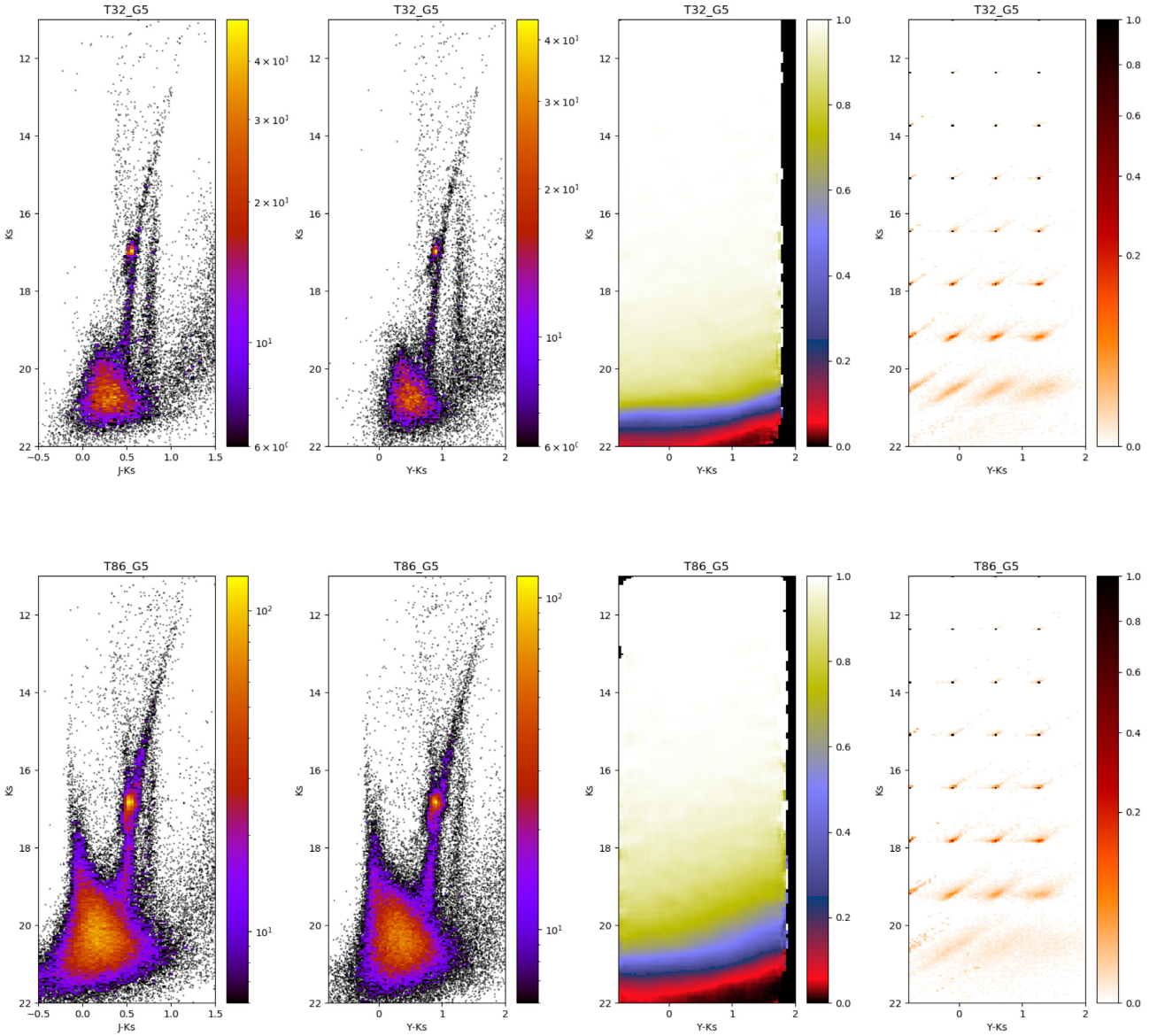

Figure 2. Examples of the observational data used for this work. The top row refers to the subregion T32_G5, located in the south-western periphery of the LMC disc. Panels from left to right show the JK_s CMD, the YK_s CMD, the completeness map for YK_s, and a sample error map in YK_s. The completeness map is filled with zeroes in regions where ASTs were not performed. The sample error map shows how points distributed on a regular grid and with initial density equal to 1 spread in the Hess diagram after convolved with their local error function. Similar diagnostic plots are available for the JK_s data set; they are not shown just for the sake of brevity – since there is no dramatic difference between the completeness and error maps in the YK_s and JK_s data sets (but for the wider colour range covered in the first case). The bottom row presents the same sequence for the subregion T86_G5, located over the Constellation III in the northern part of the LMC disc.

2.3 Characterizing photometric errors and incompleteness

As will be discussed below, we also need to assess the error function across the Hess diagrams. It is derived from large sets of artificial star tests (ASTs), namely stars injected into the original VMC images and recovered (or not) with the same PSF photometry pipeline used to derive the VMC catalogue. ASTs span the entire sky region being analysed, and are generated across the entire CMD – although with colours and magnitudes more concentrated around those of the actually observed stars. We generate a minimum number of 3×10^5 ASTs per subregion, increasing this number to $\sim 2 \times 10^6$ in some internal LMC areas more affected by crowding. They are injected in multiple runs, at random positions but avoiding self-crowding, that is, ensuring that the distances between any two artificial stars are larger than the radii involved in the PSF photometry.

Examples of completeness and error maps derived from the ASTs are presented in the right-hand panels of Fig. 2, for the YK_s data of a peripheral (top row) and of a central (bottom row) LMC region. The variation in the completeness between these two cases is evident. In addition, the right-hand panel of Fig. 1 shows a map of the K_s magnitude at which the completeness falls below 75 per cent, measured at a colour $J - K_s = 0$. This 'incompleteness map' reveals the dramatic decrease in the photometric depth of the central LMC tiles (6_6, 6_5, 6_4, 5_5, 5_6) which largely reflects the increase in the stellar density across the LMC Bar (left-hand panel of Fig. 1). Moreover, there are also noticeable tile-to-tile variations

in both stellar density and completeness, which reflect the changes in observational conditions during the 9 yr of the VMC survey.

3 THE SFH-RECOVERY METHOD

In previous works deriving the SFH from VMC data (Kerber et al. 2009; Rubele et al. 2012, 2015, 2018; Pastorelli et al. 2020) we used a method built around the StarFISH code by Harris & Zaritsky (2001). This procedure has been completely revised for this work, with the development of new and more efficient codes to derive both the best-fitting solutions and the confidence intervals of the fitted parameters, and the adoption of a different procedure to build the models. The main changes are described below, while additional details and tests are provided in a recent paper by Dal Tio et al. (2021).

3.1 General scheme

Our final goal is to identify the model **M** whose Hess diagram best reproduces the Hess diagram of the observations, **O**. This model **M** is built starting from an ideal model $\mathbf{M}_0$ resulting from a population synthesis code, which contains not only all the information about the LMC populations (distance, extinction, and SFH), but also about the MW foreground that is inevitably present in the data:

$$\mathbf{M}_0 = \mathbf{M}_0(\mathrm{SFH}, \mu_0, A_V, \mathrm{foreground}) \quad (1)$$

Many components, denoted by $\mathbf{M}_{0,i}$, are used to compute this ideal model, in the way described in Section 3.3 below.

M should also include a simulation of all relevant observational effects, including for instance the photometric errors and incompleteness. This is obtained by convolving all the individual components $\mathbf{M}_{0,i}$ with the error function for every small cell of the Hess diagram $\mathbf{E}(c, m)$:

$$\mathbf{M}_i = \mathbf{M}_{0,i} * \mathbf{E} \ . \quad (2)$$

The error function **E** is simply a matrix representation of the completeness and of the colour–magnitude offsets, at every Hess diagram bin, as derived from the ASTs (see Fig. 2 above). We typically have a few hundreds of ASTs in a single, well-populated bin of the Hess diagram. Many times more would be advisable for a high-accuracy, noiseless evaluation of the error function, but we cannot achieve that due to the computational cost of the ASTs. We instead take advantage of the slow variation of the error function across the CMDs to average them over boxes 0.24 mag wide in both magnitude and colour. This is equivalent to multiplying the number of ASTs in every bin by a factor of about 36, hence reducing the shot noise in the derivation of **E** by a factor of ∼6.

3.2 Further culling of the CMDs

Even though the above-mentioned approach can work well with a lower-than-ideal number of ASTs, on the other hand it brings a limitation to the method: it tells us that the error function cannot be trusted over CMD regions where the completeness (or the photometric errors) varies quickly with either colour or magnitude, within scales comparable to the 0.24 mag × 0.24 mag boxes within which the error functions are averaged. For this reason, we limit the SFH analyses to regions of the CMD with a completeness higher than 75 per cent at all colours. Above this limit, we are still in the regime of 'large completeness' and 'high photon counts' that ensures very smooth (close to linear) variations in the error function across ∼0.24 mag scales in the CMDs.

In addition, the SFH should be derived from CMD regions that can be reliably simulated with our present-day models, that is, using stars in the MS, subgiant branch, RGB, RC, and core-helium burning stages of intermediate and large masses. Thermally pulsing asymptotic giant branch (TP-AGB) stars should better be excluded to avoid a circular argument: even if this evolutionary phase can be well modelled with our codes, the SFH of the Magellanic Clouds was explicitly used in the calibration of the key parameters of present TP-AGB models (including their lifetimes; see Pastorelli et al. 2019, 2020). Therefore, there is no sense in using TP-AGB models in the derivation of these same SFHs. Taking these considerations into account, we further limit the SFH analysis to CMD regions with $K_s > 12$ mag, $-0.5 < Y - K_s < 1.5$ mag, $-0.5 < J - K_s < 1.0$ mag, so that:

(i) They include most of the RGB (the RGB tip is located at $K_s \sim 12.5$ mag; see Groenewegen et al. 2019) and RC stars, even in subregions with a strong reddening. In the latter cases, these features are partially superposed to the vertical feature caused by the MW foreground at $Y - K_s = 1.3$ mag and $J - K_s = 0.8$ mag.

(ii) At its brightest part, the photometry is not affected by saturation, and is not contaminated by TP-AGB stars in any significant way (see Pastorelli et al. 2020).

(iii) They exclude most of the faint background galaxies detected at redder colours ($J - K_s > 1$ mag).

(iv) They exclude the bluest part of the CMD, where hardly any star is observed.

We note that the above cuts do not entirely exclude background galaxies from our CMDs. Their complete colour–magnitude distribution, illustrated in Fig. 6 of Kerber et al. (2009), reveals a tail of faint background galaxies extending up to colours as blue as $J - K_s \sim 0.0$ mag. The impact of these galaxies in our method is evaluated in Appendix A.

3.3 The partial and total models

A total model described by equation (1) can be defined as a sum of partial models

$$\mathbf{M} = \mathbf{PM}_0 + \sum_i a_i \mathbf{PM}_i \quad (3)$$

where:

(i) $\mathbf{PM}_0$ is the partial model for the Milky Way foreground. It is computed with the calibrated TRILEGAL model (Girardi et al. 2005; Girardi 2016), whose parameters are listed in Table 1, for the coordinates and total area under consideration. Foreground extinction is ignored since it is expected to be smaller than 0.2 mag in A_V (Subramaniam & Subramanian 2010), hence affecting the K_s, $Y - K_s$ and $J - K_s$ data by less than 0.024, 0.054, and 0.033 mag, respectively. Such changes are much smaller than the MW foreground features observed in VMC data and predicted by TRILEGAL models.

(ii) $\mathbf{PM}_i$ are the partial models computed for the LMC, for 16 age bins, and following a given initial age–metallicity relation (AMR) $[\mathrm{Fe/H}]_0(t)$, and for a reference value of true distance modulus and extinction, namely $\mu_0 = 18.5$ mag and $A_V = 0$ mag.[3] For convenience, all the $\mathbf{PM}_i$ represent stellar populations formed at a constant star formation rate of $\mathrm{SFR}(t) = 1 \mathrm{M}_\odot \mathrm{yr}^{-1}$, inside the age limits of every

[3] $\mu_0 = 18.5$ mag is a classical value for the true distance modulus of the LMC centre (Freedman et al. 2001; Pietrzyński et al. 2009), differing very little from more recent and accurate determinations (e.g. Pietrzyński et al. 2019).

Table 1. Parameters used in the TRILEGAL model to compute the MW foreground. The notation is the same as in Pieres et al. (2020), while the meaning of each parameter is thoroughly described in Girardi et al. (2005) and, specifically for the bulge component, in Vanhollebeke, Groenewegen & Girardi (2009).

Component	Parameter identifier	Parameter value
Sun's position	$R_\odot$	8700 pc
	$z_\odot$	24.2 pc
Thin disc	$\Sigma_\odot^{\rm thin}$	55.41 $M_\odot$ pc^{-2}
	$h_R^{\rm thin}$	2913 pc
	$h_{z,0}^{\rm thin}$	94.7 pc
	$t_{\rm incr}^{\rm thin}$	5.55 Gyr
	α	1.67
Thick disc	$\rho_\odot^{\rm thick}$	0.0010 $M_\odot$ pc^{-3}
	$h_R^{\rm thick}$	2394.07 pc
	$h_z^{\rm thick}$	800 pc
Halo	$\rho_\odot^{\rm halo}$	0.0001 $M_\odot$ pc^{-3}
	$r_{\rm eff}$	2698.93 pc
	$b_{\rm h}$	0.62
	$n_{\rm h}$	2.75
Bulge	$\rho_{\rm GC}^{\rm bulge}$	406 $M_\odot$ kpc^{-3}
	$a_{\rm m}$	2500.0 pc
	a_0	95.0 pc
	$1{:}\eta{:}\zeta$	1:0.68:0.31
	ϕ_0	15°

bin. Therefore, the coefficients a_i can be directly read as the SFR(t) in these units.

Then, there are small corrections to this model that allow us to explore small shifts in the global LMC properties, in a fast way:

(1) The model can be computed with a given colour–magnitude shift in the Hess diagram, (Δc, Δm), being applied to all the $\mathbf{PM}_i$ components. This shift is intended to reproduce the shifts caused by changes in the mean reddening and distance modulus of the individual LMC subregions, with respect to the reference values used to compute the PMs. It can also compensate small errors in the photometric zero-points (although such a compensation is not applied to the MW foreground, as it should be in the case it were really caused by errors in the photometric zero-points). To improve the efficiency of our algorithms, the (Δc, Δm) changes are computed only for a limited set of values, which are integer multiples of the resolution in the CMD. For any non-integer multiple, CMDs are computed as a bilinear interpolation of the CMDs for the four neighbouring points in (Δc, Δm) space. This allows us to compute models at runtime, for arbitrary (Δc, Δm) shifts, with just a factor 4 increase in computing time with respect to the standard ($\Delta c = 0$, $\Delta m = 0$) case. We typically allow the code to explore intervals of 0.28 mag in both Δc and Δm.

(2) At all ages, partial models are computed for four additional metallicities, differing by Δ[Fe/H] = (-0.16, -0.08, $+0.08$, $+0.16$) dex with respect to the reference AMR. This allows us to compute a model for an arbitrary metallicity shift, Δ[Fe/H], using linear interpolation among the two models which bracket its metallicity. Notably, this method allows us to consider small continuous shifts in metallicity by just doubling the computing time, compared to the fixed-AMR case.

These are crude approximations that could be replaced by the actual computation of models at many intermediate values of (Δc, Δm, Δ[Fe/H]). This, however, would imply a huge increase in computing time, and impose large amounts of computer memory being allocated for increased sets of 'shifted partial models', effectively prohibiting us the use of Markov chain Monte Carlo (MCMC) methods in our derivation of the SFH solution (cf. Section 3.6).

Moreover, we could decide that the metallicity shifts Δ[Fe/H] assume independent values for every age interval i, hence exploring a wide area of the age–metallicity plane. However, changes in the mean AMR of a galaxy field are expected to take place over timescales of Gyr, which excludes large metallicity variations between any two neighbouring age bins in our sequence of young PMs. It should also be noted that the more parameters we use to describe metallicity shifts at different ages, the longer the SFH-recovery process (see Section 3.6) takes to explore the available parameter space. To limit the metallicity variations to a subset of astrophysically plausible variations, while using few parameters to describe them, we define two Δ[Fe/H] coefficients at the extreme youngest and oldest ages: Δ[Fe/H]$_1$ and Δ[Fe/H]$_2$. Δ[Fe/H] values for all ages are then computed as a simple linear interpolation between these two extremes, with linear age, t_i, as the interpolation parameter. In this way, the value of Δ[Fe/H]$_1$ applies to all young populations, mainly affecting the position of the MS stars, while Δ[Fe/H]$_2$ starts affecting the populations older than a few Gyr, hence mainly affecting the properties of the subgiants and giants in the CMD. As before, this simple scheme represents a compromise in which small variations in our input models are explored, but avoiding changes that would imply large increases in the usage of computing time and computer memory.

3.4 Computing PMs with TRILEGAL

For the LMC, we adopt the reference AMR taken from the 'closed-box model $y = 0.08$' from Carrera et al. (2008), which compares very well with their age–metallicity data for LMC field stars. The main characteristics of this AMR is the presence of two main periods of chemical enrichment, the first one at early epochs exceeding ∼6 Gyr, the second one at ages younger than 3 Gyr. They are separated by a period of slower increase in metallicity that corresponds to a period of reduced cluster and field star formation in the LMC disc (see also Carrera et al. 2011). In addition to this reference AMR, we assume that the metallicities have an intrinsic Gaussian dispersion of σ = 0.05 dex at all ages.

As for the stellar models, we adopt the PARSEC tracks v1.2S (Bressan et al. 2012; Chen et al. 2014, 2015), in the form of the isochrones provided by default in the CMD web interface version 3.3.[4] These models have been used in a series of previous works on the VISTA and 2MASS (the Two Micron All-Sky Survey; Skrutskie et al. 2006) near-infrared photometry of Magellanic Cloud populations, generally with good results (e.g. Lebzelter et al. 2018; Rubele et al. 2018; Pastorelli et al. 2019, 2020; Trabucchi et al. 2019, 2021). Mass-loss between the tip of the RGB and the core-helium burning phase is taken into account with an efficiency of 0.2 times the value provided by the Reimers (1975) formula (see Miglio et al. 2012). Since our reference AMR extends to very small metallicities (reaching [Fe/H] = −3.2 dex at the oldest assumed age of 15 Gyr), these models also include metal-poor populations rich in horizontal branch stars. The theoretical models are converted into the VISTA photometry, in a Vegamag system, via the transformations described by Chen et al. (2019); for the stars we model in this work, they are largely based on grids of model atmospheres and synthetic spectra by Castelli & Kurucz (2003) and Husser et al. (2013).

[4] http://stev.oapd.inaf.it/cgi-bin/cmd_3.3

Table 2. Age bins adopted, with their corresponding metallicity interval.

i	$\log(t/\mathrm{yr})$	Δt (yr)	$[\mathrm{Fe/H}]_0$ interval (dex)
1	6.6, 6.9	3.96×10^6	−0.19, −0.19
2	6.9, 7.2	7.91×10^6	−0.19, −0.19
3	7.2, 7.5	1.58×10^7	−0.19, −0.19
4	7.5, 7.8	3.15×10^7	−0.19, −0.19
5	7.8, 8.1	6.28×10^7	−0.19, −0.19
6	8.1, 8.4	1.25×10^8	−0.19, −0.19
7	8.4, 8.6	2.50×10^8	−0.19, −0.19
8	8.6, 8.8	2.32×10^8	−0.19, −0.19
9	8.8, 9.0	3.69×10^8	−0.19, −0.19
10	9.0, 9.2	5.85×10^8	−0.19, −0.25
11	9.2, 9.4	9.17×10^8	−0.25, −0.36
12	9.4, 9.6	1.47×10^9	−0.36, −0.49
13	9.6, 9.8	2.33×10^9	−0.49, −0.60
14	9.8, 10.0	3.69×10^9	−0.60, −0.95
15	10.0, 10.1	2.59×10^9	−0.95, −2.07
16	10.1, 10.2	3.26×10^9	−2.07, −3.18

We adopt the canonical initial mass function (IMF) from Kroupa (2001, their eqs. 1 and 2; see also equation (4.55) of Kroupa et al. 2013). Binaries are considered only in the form of detached systems, assuming that 30 per cent of the stars drawn from the IMF have a companion, with a mass ratio between 0.7 and 1. This prescription suffices to produce a secondary MS parallel to that caused by single stars, and similar to the one observed in *HST* photometry of star clusters (see e.g. Sollima et al. 2007). The IMF is normalized so that its integral from 0.01 to 250 $\mathrm{M}_\odot$, taking into account both single and binary systems, produces a total mass of 1 $\mathrm{M}_\odot$.

We create PMs for 16 age bins (see Table 2), at almost-regular intervals of $\log(t/\mathrm{yr})$, but with widths that become narrower for older populations: bins are 0.3 dex wide starting at $\log(t/\mathrm{yr}) = 6.6$, and becoming 0.2 dex wide after $\log(t/\mathrm{yr}) = 8.4$. Moreover, after $\log(t/\mathrm{yr}) = 10.0$ we have two bins 0.1 dex wide, which have very similar Hess diagrams, but with the oldest age bin having a much more extended horizontal branch. The reason for adopting wider age bins at younger ages is essentially to reduce the errors in the determination of the SFH, as discussed in Kerber et al. (2009).

3.5 The model likelihood

Summarizing, with these choices, a model is determined by (1) the region coordinates, which define the foreground model $\mathbf{PM}_0$, and (2) a set of variable parameters that define the LMC populations. The latter comprise

(i) the coefficients for 16 age bins, a_i, representing the mean SFR(t) in every age interval;

(ii) a global shift in the CMD in both colour and magntiude, (Δc, Δm), which is intended to reproduce the shifts caused by reddening and changes in distance modulus (with respect to the reference values used to compute PMs), and/or small errors in the photometric zero-points;

(iii) metallicity shifts $\Delta[\mathrm{Fe/H}]_1$ and $\Delta[\mathrm{Fe/H}]_2$, representing small changes in mean metallicity at the extreme ages, which affect the final AMR at all ages.

Given this model, for the model-data comparison we adopt the following definition of likelihood ratio derived from a Poisson distribution:

$$\ln \mathcal{L} = \sum_k \left(O_k - M_k - O_k \ln \frac{O_k}{M_k} \right) \quad (4)$$

(Dolphin 2002; Vanhollebeke et al. 2009), where O_k and M_k are the observed and model star counts, respectively, in all CMD bins of index k not masked by our selection criteria of Section 3.2. For all CMD bins in which there is a significant number of observed and model stars, results are similar to half of the classical χ^2 (or Gaussian likelihood ratio), where the standard deviation is given by the square root of the observed star counts (see the discussion in Dolphin 2002).

3.6 Finding the best solutions

The search for the maximum-likelihood model is performed in two steps. The first one is a Nelder–Mead minimization based on the Press et al. (1992) routine, which quickly adjusts the a_i coefficients while keeping all the other parameters fixed (which is equivalent to assuming null shifts in metallicity, distance, and reddening). This approximate solution provides an initial model for a Metropolis–Hastings MCMC (Metropolis et al. 1953), where all parameters are allowed to vary. As a rule, the MCMC is performed with 500 walkers and in 8000 steps, using a new C code (namely `trifit`; see Dal Tio et al. submitted) built according to the guidelines from Hogg & Foreman-Mackey (2018).

Our best-fitting solution is represented by the complete set of final walkers positions. From these, we determine the median, and 68 per cent and 95 per cent confidence intervals of all parameters. Appendix C describes the machine-readable tables that are available. We also produce the mean Hess diagram from the final walkers, which is then compared to the observed one. Examples of solutions are provided in the summary plots of Figs 3 and 4.

For a few subregions, we ran much longer MCMCs (up to 100 000 steps), without finding any significant reduction in the final values of $-\ln \mathcal{L}$ or changes in the derived parameters. We also tried setting our initial guesses for a_i at different threshold values, in age bins for which the Nelder–Mead step was indicating null values. In all cases the MCMCs converged to the same final set of parameters values, within their 95 per cent confidence intervals. We therefore consider the minimization process to be robust.

One caveat is worth of mention at this point: looking at the final distribution of median parameters for all subregions, we notice a concentration of the (Δc, Δm) values on a grid with an approximate spacing of 0.04 mag × 0.04 mag, for both the JK_s and YK_s data sets. Also, the final walkers for every subregion concentrate on a similar grid, but sometimes with sub-concentrations appearing with a different spacing (as small as ∼0.02 mag). This 'grid effect' probably results from the adoption of bilinear interpolations to estimate models at intermediate values of (Δc, Δm). These interpolations are extremely quick to compute and produce the continuous variation of the $\ln \mathcal{L}$ values that is required by the MCMC code, but introduce discontinuities in the derivatives of $\ln \mathcal{L}$ at the borders of the grid cells. They also produce 'saddles' in the $\ln \mathcal{L}$ values near the central spots of the grid, hence creating regions in (Δc, Δm) space where the solutions can accumulate. Eliminating this effect implies either adopting a finer grid of models, or alternative interpolation algorithms, in both cases with a significant cost in terms of computing time. For the moment, we simply prefer to accept these errors, considering them as systematic errors in the derivation of our extinction and distance values (see Sections 4.4 and 4.5).

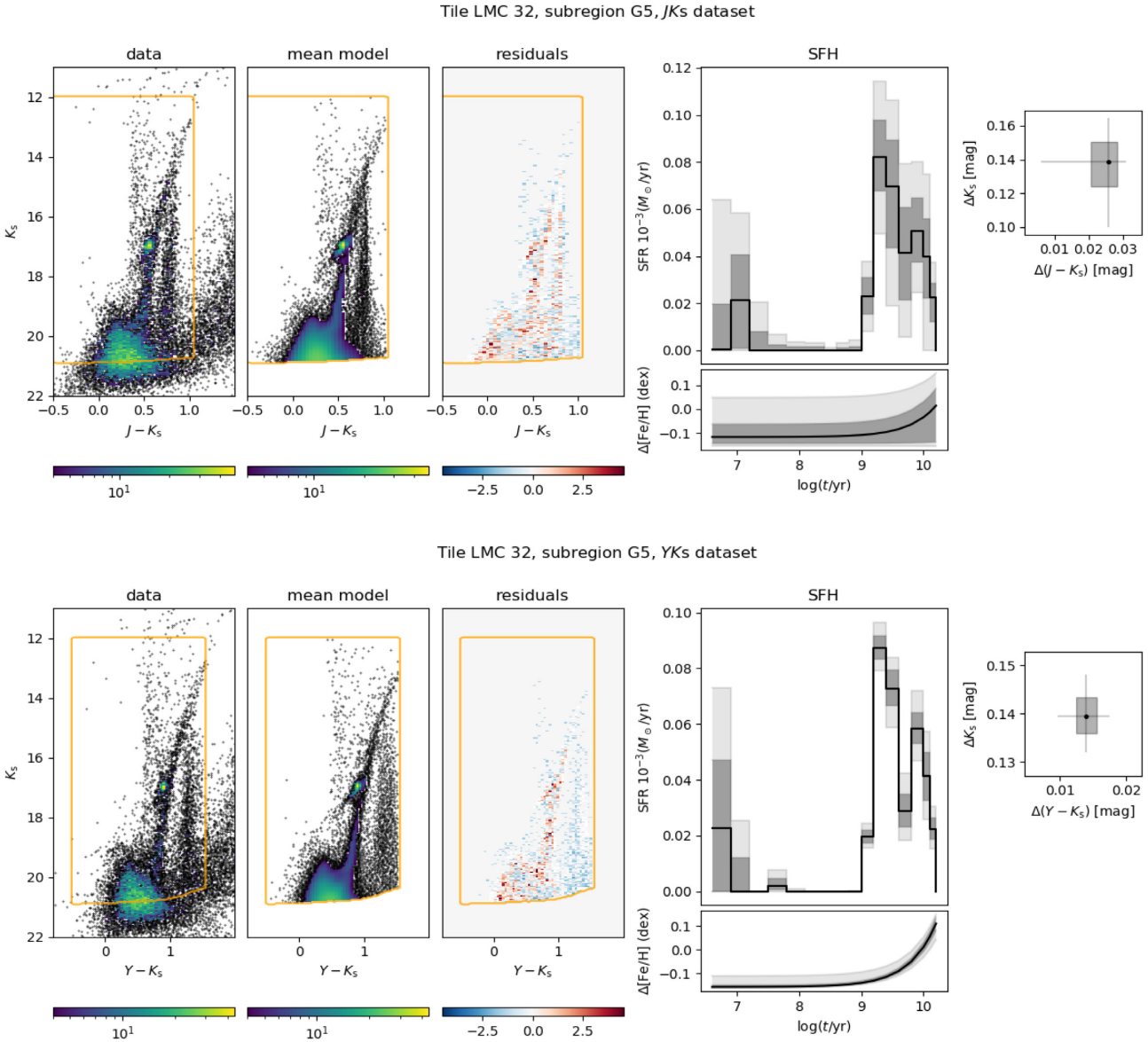

Figure 3. Summary plots presenting the results of fitting the JK_s and YK_s data (top and bottom rows, respectively) of subregion T32_G5. The three panels from left to centre show the Hess diagrams of the data, of the mean MCMC solution, and finally the residual between the first two panels, in units of σ. Note that the models are computed only for the CMD area inside the orange line, which takes into consideration our colour–magnitude cuts and the adopted threshold in completeness. Moreover, the 'mean model' is represented in an idealized way, with individual stars being randomly simulated in regions of low density, so that it can be plotted in the same way as the actual observations; the actual mean model instead is a Hess diagram containing ample areas with lower-than-unity values. The rightmost panels show the results in terms of the fitted parameters, and the astrophysical quantities they represent. These results include the SFH, which is made of (1) the SFR(t) in units of $M_\odot yr^{-1}$ plus (2) the [Fe/H] differences with respect to our reference values, for which we plot the median values (dark lines), and their 68 per cent and 95 per cent confidence intervals (grey and light-grey areas, respectively). Finally, the results include (3) the colour–magnitude shifts with respect to the reference initial value, which are shown in the rightmost panel, with median value (dot) plus 68 per cent and 95 per cent confidence intervals (grey box and light-grey error bars, respectively).

4 RESULTS FOR ALL SUBREGIONS

4.1 The SFH maps

Examples of our solutions, derived independently from the JK_s and YK_s data sets, are provided in Figs 3 and 4. Comparing the different cases one immediately notices that the SFHs derived from JK_s and YK_s are qualitatively (if not quantitatively) very similar, except for very young ages ($\log(t/yr) < 7.2$).

For most of the subregions, the mean model solutions are remarkably similar to the real data in the Hess diagrams. But looking at the map of residuals, some discrepancies appear concentrated in small CMD regions, for instance around the RC. Moreover, the models tend to present the LMC features slightly sharper than in the data, whereas the model MW features sometimes are more spread in colour than the data (especially in $Y - K_s$). Actually, we find that many of these discrepancies could disappear from our sight if we were to plot the data with colour–magnitude bins twice as large as

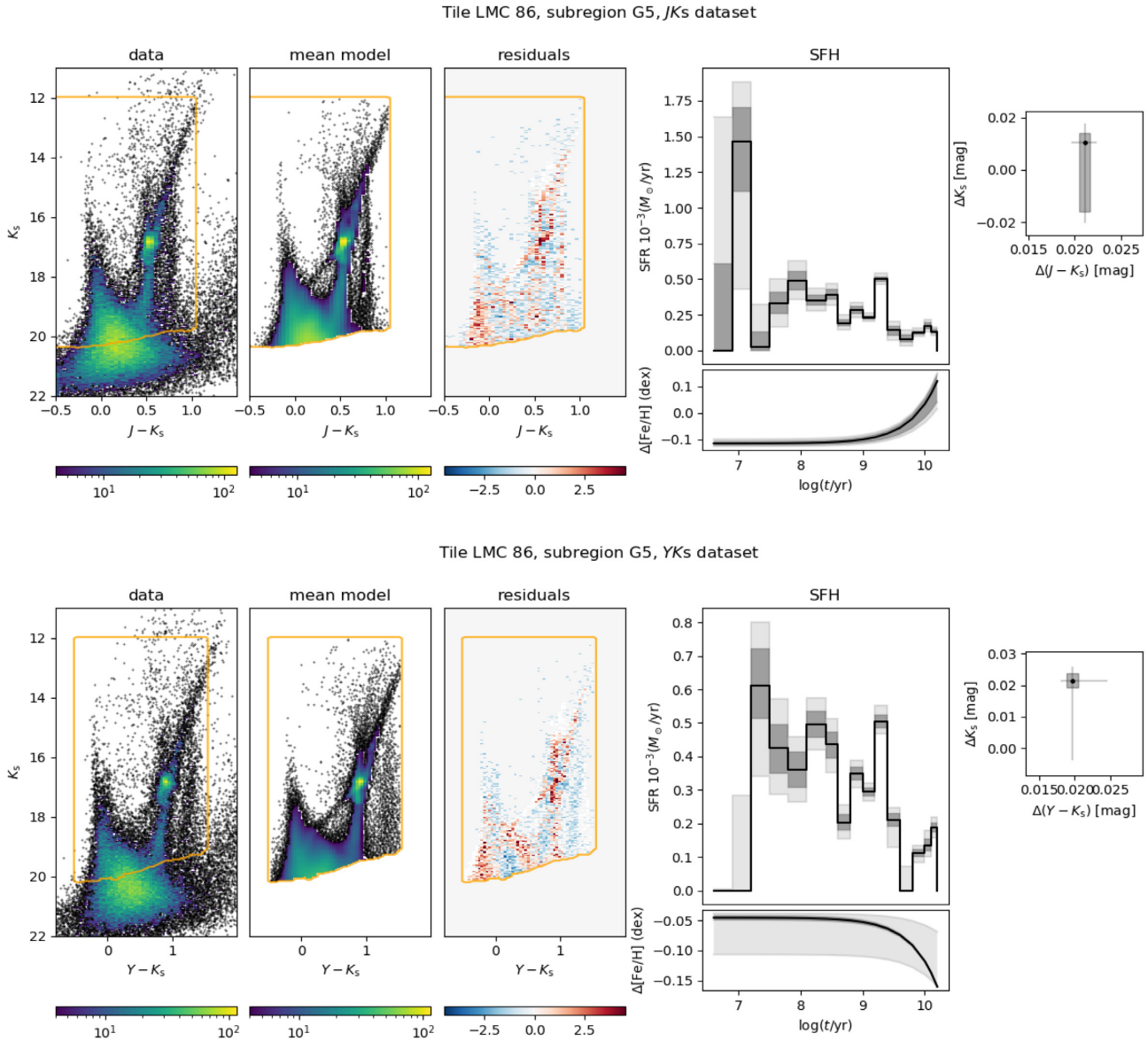

Figure 4. The same as Fig. 3, but for the T86_G5 subregion.

their present size, or if we were to plot the single model with the maximum likelihood instead of the mean model derived from all final walkers. These discrepancies could be attributed to a series of problems, going from deficiencies in stellar models to the imperfect simulation of astrophysical effects (e.g. a possible intrinsic dispersion in extinction and distance) and observational effects (e.g. possible inaccuracies in the zero-points, insufficient ASTs, etc.). Investigating these possibilities would be very demanding both computationally and in terms of the effort required to properly assess the effects of each one.

Let us now take a look at the whole picture obtained combining all the solutions, that is, at the SFH maps of Figs 5 and B1, which present the spatial distribution of the inferred SFR(t) at all age intervals. A few features are immediately evident in these plots:

(i) The patchy distribution of SFR(t) for all ages younger than about 63 Myr (first row in the figures). At these ages, the SFR(t) strongly varies from subregion to subregion, and the only large-scale feature is the concentration in a central disc of diameter ∼7 deg.

(ii) At older ages, the SFR(t) is more smoothly distributed, and becomes more extended as age increases. A notable aspect of these maps is that the SFR(t) is concentrated on the LMC bar, and in (at least) three well-defined spiral arms clearly visible, for example, in the age bin 8, two to the north of the bar and one to the south of it. These configurations persist until ages of at least 1.6 Gyr – but with the spiral arms becoming progressively less prominent with increasing age.

(iii) For even older ages, the central bar becomes less and less defined, until the SFR(t) maps eventually reveals a wide, nearly spheroidal structure distributed over a diameter exceeding 10 deg, for ages older than ∼1.6 Gyr. A clear problem then appears, starting at about the same ages: the maps present a number of holes, corresponding to either isolated subregions, or to groups of neighbouring subregions, where the median SFR(t) falls to values close to null. These are either subregions where the old SFR(t) presents very large errors (in practice, we are deriving just an upper limit to the SFR(t)), or where the SFH-determination method fails to find astrophysically reasonable solutions. The subregions affected

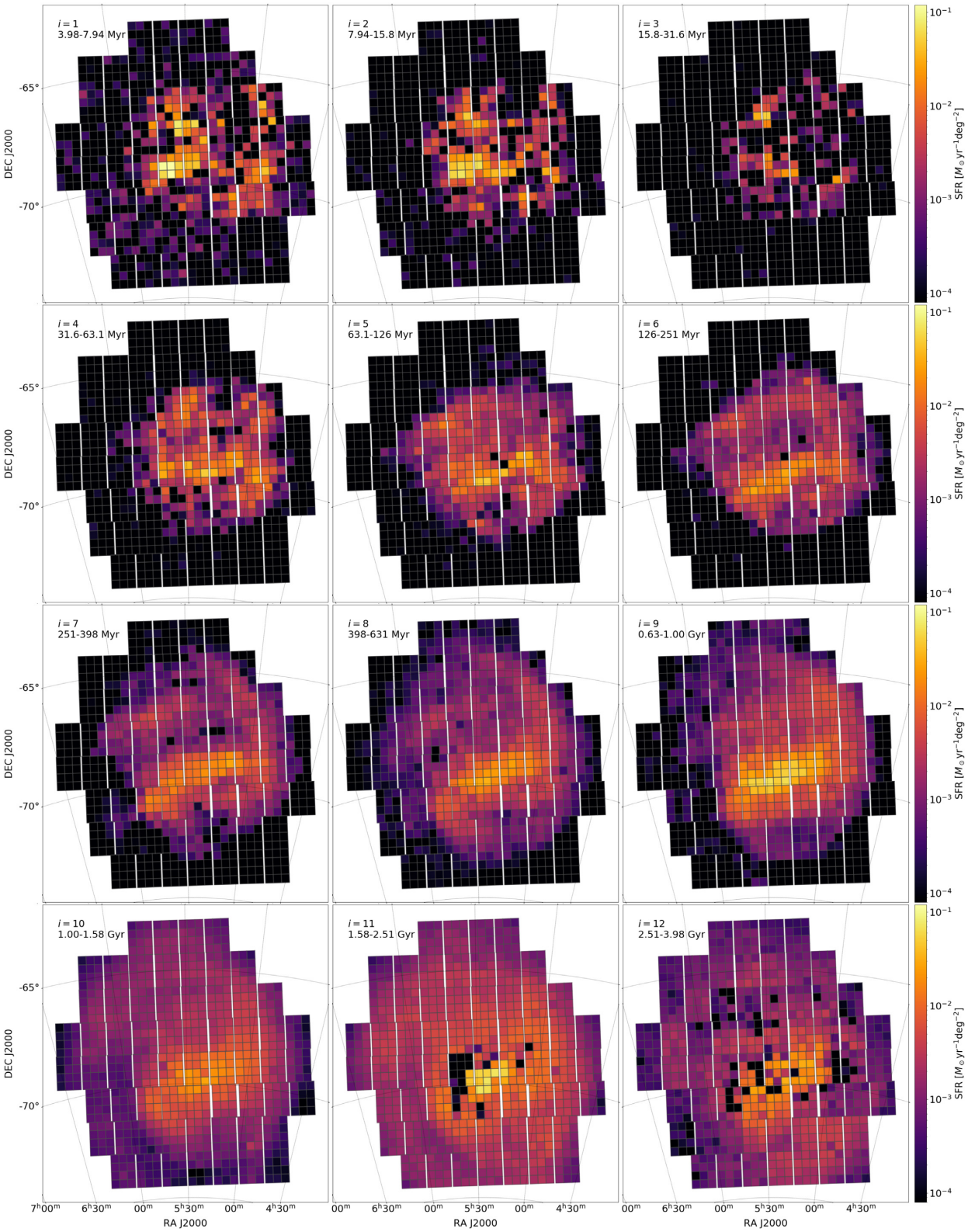

Figure 5. SFR(t) maps from derived the JK_s data. The 16 panels present the median value of the SFR(t) in units of $M_{\odot}yr^{-1}$ divided by the effective area of every subregion, for all our age bins. The colour scale is the same in all panels.

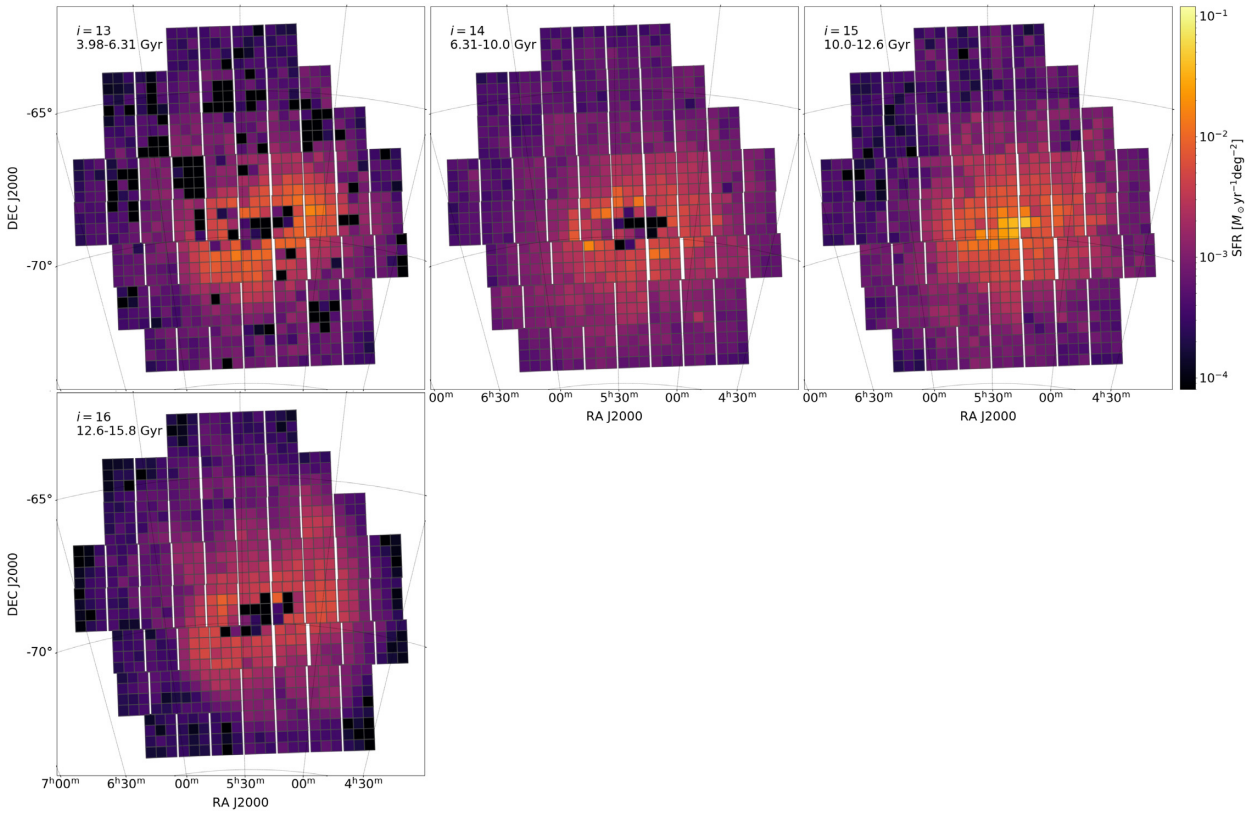

Figure 5 - *continued*.

are often associated with large amounts of differential extinction (see Section 4.4) and/or extreme crowding.

It is probably no coincidence that the latter problem starts at the 1.6 Gyr ages in which the RGB and RC develop in stellar populations. Starting at that age, the information about the SFR(t) comes less and less from the dimming turn-off and subgiant branch, and more and more from the RGB and RC regions of the CMD. The RGB and RC are notorious for being very concentrated in the CMD and even more so in NIR CMDs. It is enough to have these two features blurred by differential extinction to lose much of the age information they contain. Interestingly, the SFR(t) for age bin number 15 appears remarkably smooth in these maps; it is associated with old populations with a short horizontal branch, which do not concentrate in the CMD as much as the RC.

Can we tell in advance, just looking at the final likelihood of the fit, what are the subregions for which the old SFR(t) is unreliable? This is not so easy. However, the maps of likelihood, presented in Fig. 6, do indicate several regions of higher-than-average $-\ln \mathcal{L}$, and many of them (but not all) coincide with holes in the old-SFR(t) maps.

Another aspect to consider is that the holes in the SFR(t) maps at certain ages are, at least partially, compensated by a higher SFR(t) at neighbouring age intervals. This is because the fitting algorithm will always try to produce RGB and RC stars in appropriate numbers to fit the CMD. Whenever the extinction is moderate, the stars more suitable to produce these appropriate numbers will likely be found in nearby age intervals – but not at age intervals with $<$1.5 Gyr, which have dramatically different CMD features.

These problems could probably be solved by using additional data – for instance detailed maps of internal reddening, or CMDs from optical data being analysed simultaneously with the VMC data – in the CMD-fitting method. Such options will be explored in subsequent papers.

4.2 Consistency checks on the SFR(t)

As a consistency check, we compare our maps with the distribution of stars expected to be contained into small age intervals. The first case is offered by RR Lyrae, which were formed $\gtrsim$10 Gyr ago, and preferably at low metallicities. Fig. 7 compares the mean SFR(t) for ages $>$10 Gyr as obtained from the JK_s data (see the two last panels of Fig. 5), with the absolute number of RR Lyrae in each subregion from the catalogue by Cusano et al. (2021). Additional plots regarding the spatial distribution of the RR Lyrae, and the SFR(t) derived from YK_s, are presented in Fig. B2. It is evident that the spatial scale of the RR Lyrae and old SFR(t) distributions are very similar. The mean proportionality constant between these quantities is of 1.58×10^5 and 1.45×10^5 RR Lyrae $M_\odot{}^{-1}$yr for the YK_s and the JK_s maps, respectively. Of course, this relation is influenced by a few of the central subregions, which have high but potentially incomplete numbers of RR Lyrae, and whose SFR(t) estimates are more affected by crowding and differential reddening. It is also evident that the points in the diagram are more spread than expected from the formal error bars. Overall, this plot is reassuring (because there is a clear correlation), but also indicates that there is space for improvement in the determination of the old SFR(t).

Fig. 8 presents the same kind of comparison for the classical Cepheids from the catalogue by Ripepi et al. (in preparation). Their distribution is compared to the SFR(t) at the sixth age bin, corresponding to ages between 126 and 251 Myr. This is the age interval at which the blue extremity of the 'blue loop' of core-helium burning stars transits from the red to the blue of the instability strip,

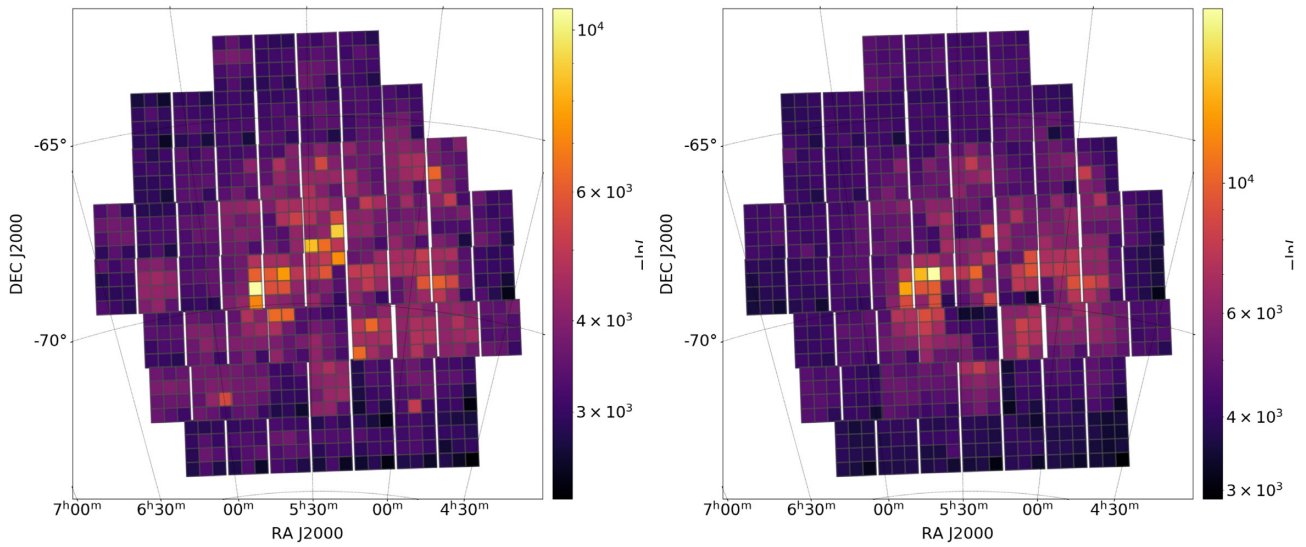

Figure 6. Maps of likelihood, $-\ln \mathcal{L}$, for the JK_s (left) and YK_s (right) solutions.

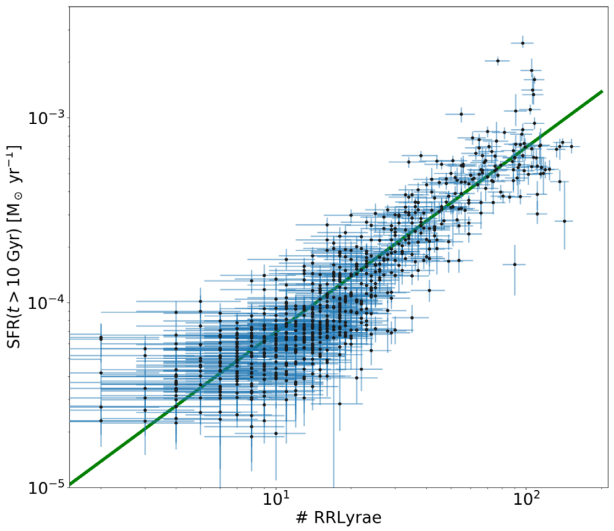

Figure 7. Comparison between the SFR(t) at very old ages, derived from JK_s data, with the number of RR Lyrae in each subregion. The error bars correspond to the 68 per cent confidence interval of the SFR, and to the square root of star counts. The green line presents the mean relation derived assuming a perfect proportionality between these quantities: its slope is of 1.45×10^5 RR Lyrae per unit $M_\odot yr^{-1}$.

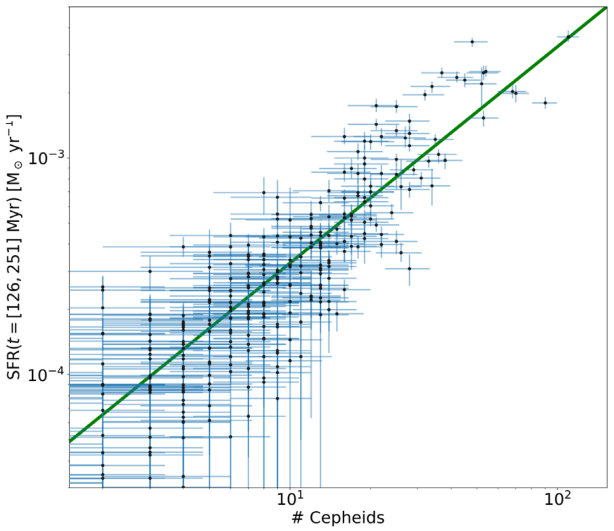

Figure 8. Comparison between the SFR(t) at ages between 126 and 251 Myr, derived from the JK_s data, with the number of Cepheids in each subregion. The error bars correspond to the 68 per cent confidence interval of the SFR, and to the square root of star counts. The green line presents the mean relation derived assuming a perfect proportionality between these quantities: its slope is of 3.07×10^4 Cepheids per unit $M_\odot yr^{-1}$.

producing the maximum numbers of Cepheids for a given SFR. Additional plots regarding the spatial distribution of the Cepheids, and the SFR(t) derived from YK_s, are presented in Fig. B3. Also in this case, there is an evident correlation between the number of Cepheids and our derived SFR(t). The correlation is somewhat noisy and may be affected by the strong differential extinction of some central LMC subregions. The mean proportionality constant is 3.03×10^4 and 3.07×10^4 Cepheids $M_\odot{}^{-1}yr$, for the YK_s and the JK_s maps, respectively.

4.3 Correction to photometric zero-points

Our PSF photometry is based on the v1.3 calibration of VISTA data. When our analysis of the SFH was well underway, we measured the offsets between this photometry and the more accurate v1.5 calibration from González-Fernández et al. (2018), on a tile-to-tile basis. They imply corrections to the PSF photometry whose mean and r.m.s. values, for our 63 tiles, are

$$\begin{aligned} \Delta zp(K_s) &= 0.000 \pm 0.017 \text{ mag} \\ \Delta zp(Y-K_s) &= -0.026 \pm 0.026 \text{ mag} \\ \Delta zp(J-K_s) &= 0.026 \pm 0.022 \text{ mag} \end{aligned} \quad (5)$$

These corrections are typically smaller than our adopted CMD resolution, and much smaller than the total shifts in colour and magnitude that we explore during the CMD fitting. Therefore, instead of using them to correct the input photometry, these zero-point shifts are added, a posteriori, as small corrections to the (Δc, Δm) derived in our CMD fitting. Then, we can define the following 'magnitude

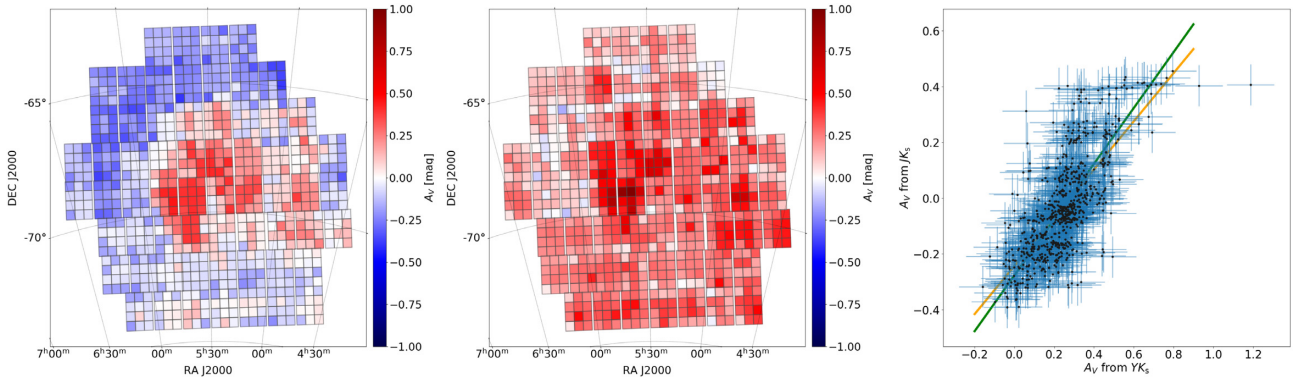

Figure 9. *V*-band extinction maps derived from YK_s (left-hand panel) and JK_s (central panel) data. The right-hand panel shows the relationship between them, with two fitted relations: a systematic shift of $A_V^{YK_s} = A_V^{JK_s} - 0.28$ mag (green), or a best-fitting line of $A_V^{YK_s} = 0.86\,A_V^{JK_s} - 0.24$ (orange).

and colour excesses':

$$\begin{aligned} E(K_s) &= \Delta m + \Delta zp(K_s) \\ E(Y-K_s) &= \Delta c^{YK_s} + \Delta zp(Y) - \Delta zp(K_s) \\ E(J-K_s) &= \Delta c^{JK_s} + \Delta zp(J) - \Delta zp(K_s) \end{aligned} \quad (6)$$

which are necessary to explore the extinctions and distances across the LMC.

4.4 Extinction maps

Assuming a Cardelli, Clayton & Mathis (1989) extinction law, extinction coefficients of an average dwarf star (the Sun) at the limit of low extinction are

$$(A_Y, A_J, A_{K_s}) = (0.391, 0.288, 0.120)\,A_V\,. \quad (7)$$

(see Girardi et al. 2008; Rubele et al. 2012). These coefficients change little for stars of different effective temperature and surface gravity; for instance they decrease by less than 2 per cent for cool RGB stars of $T_{\rm eff} = 3500$ K, $\log g[{\rm cm\,s^{-2}}] = 0.5$. Slightly larger are the variations between coefficients published by different authors, due to the way filter transmission and extinction curves are interpolated and convolved, and to changes in the exact definition of 'low extinction'.[5] Such variations are inconsequential for this work, and they are similar to the differences among coefficients derived from different extinction curves in the literature.

Our CMD-fitting solutions provide the colour excesses (equation 6) which we equal to the colour excess caused by interstellar dust. They can be converted into the total extinction with:

$$\begin{aligned} A_V &= 3.69 \times E(Y - K_s) \\ A_V &= 5.95 \times E(J - K_s) \end{aligned} \quad (8)$$

providing two independent values of A_V. They are plotted in the form of extinction maps in Fig. 9. We choose a representation using A_V because it can be easily compared with the many extinction maps already present in the literature. Some readers could prefer a representation using A_{K_s}, which is easily obtainable by multiplying the colour scale of Fig. 9 by 0.12.

As for the errors in A_V, they derive directly from the errors in the colour excess in equation (8). They have two components, which we add in quadrature: the first is the 68 per cent confidence intervals of Δc provided by the MCMC method. The second is half the stepsize in colour of our Hess diagrams, that is, 0.02 mag. This latter is assumed as a minimum error, necessary to take into account the grid effect we find in our final Δc values (see Section 3.6).

Negative extinction values do occur in Fig. 9, and by itself they are indicating that factors other than extinction are contributing to the colour shifts. Likely candidates are offsets in the evolutionary models, which would affect all tiles, and additional (unidentified) offsets in the photometric zero-points, whose effect could also appear on a tile-to-tile basis. Indeed, we find that:

(i) The A_V map derived from JK_s has just a few peripheral regions with slightly negative values, down to $A_V = -0.2$ mag. Positive values extend up to $A_V = +1.2$ mag.

(ii) In the A_V map derived from YK_s, instead, nearly half of the subregions have negative values. The A_V values extend all the way from -0.4 to $+0.45$ mag.

(iii) There is a correlation between the two A_V values, with a weighted least-squares fit producing either a systematic shift of $A_V^{YK_s} = A_V^{JK_s} - 0.28$ mag, or a best-fitting line of $A_V^{YK_s} = 0.87\,A_V^{JK_s} - 0.24$ mag.

The most natural interpretation of these results is that either there is an error in the extinction coefficients applied to the different filters, or there is a systematic error affecting the photometry, *either in the data or in the theoretical models*. In this regard, we note that (1) our adopted extinction coefficients (equation 7) in the VISTA JK_s passbands agree with those determined for 2MASS JK_s passbands in a series of empirical methods (Indebetouw et al. 2005; Zasowski et al. 2009; Wang & Jiang 2014; Schlafly et al. 2016), (2) the VMC data are strictly calibrated using 2MASS data, which does not have a *Y* filter, and finally (3) the model fitting produces reasonable A_V values when only JK_s data are used. All these factors lead us to conclude that the problem is more likely associated with the *Y* filter, than with the JK_s ones. Indeed, all results would become more reasonable if the *Y*-band photometry was shifted by $+0.07$ mag, or alternatively, if all model *Y*-band magnitudes were shifted by -0.07 mag.

The range of parameters adopted (Section 3.3) allows us to explore A_V values in the approximate ranges $[-0.45, +0.59]$ mag for YK_s data, and $[-0.48, +1.20]$ mag for JK_s data. In the case of YK_s data, about 20 subregions reached values close to the upper A_V limit, but only in central regions severely affected by crowding, which will be eliminated from most of our discussion further below.

[5]For instance, Chen et al. (2019) recently derived extinction coefficients smaller by a few per cent, i.e. (0.369,0.272,0.118), using the same Cardelli et al. (1989) extinction curve.

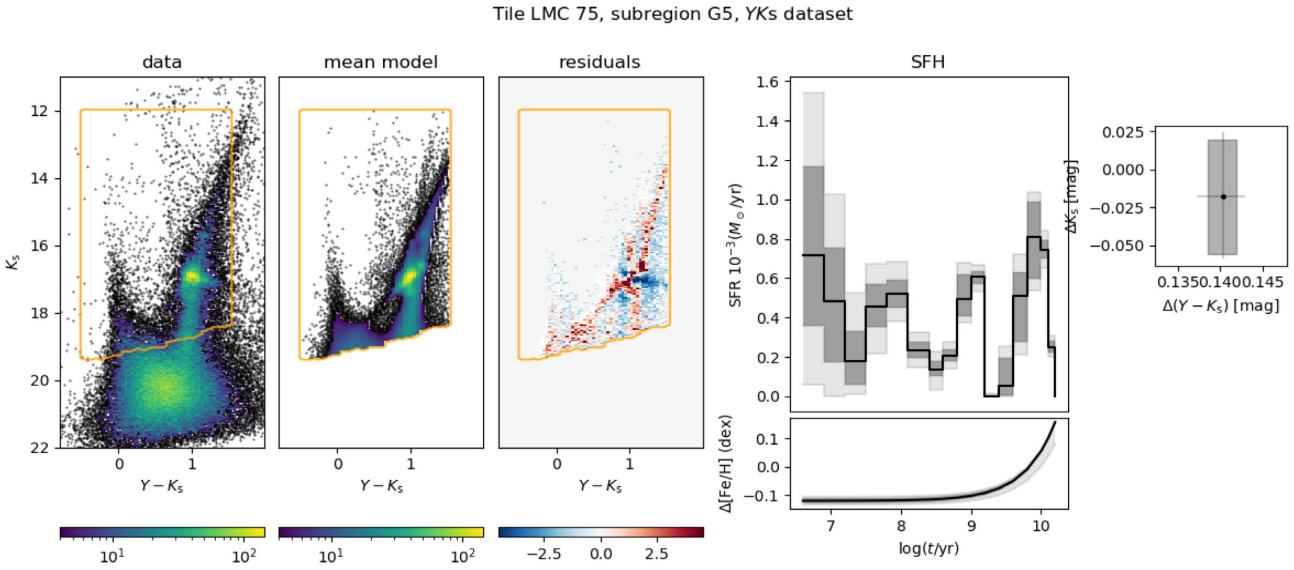

Figure 10. The same as Fig. 4, but for the YK_s data of the highly extincted subregion T75_G5.

In some subregions, VMC photometry provides significant evidence for a large internal spread in the extinction values. An example is provided in Fig. 10, for the subregion T75_G5. Its Hess diagram presents an extended tail of reddened RC stars, rather than a simple shift of the RC to redder colours and fainter magnitudes. They are indicating that extinction is rapidly varying across the subregion, and possibly also varying in depth across the LMC disc. Other examples are given in Tatton et al. (2013), who better illustrate the spatial scale at which such extended RC tails appear. Our present models are not built to reproduce this kind of situation. Indeed, the mean models illustrated in Fig. 10 fail to fit the shape of the RC and present high residuals in other parts of the CMD as well. The unsuitability of this model fit is evidenced by the increased $-\ln \mathcal{L}$ in the likelihood maps of Fig. 6. Other examples of subregions with highly non-uniform extinction are T85_G7, T75_G10 (rich in pre-main-sequence stars; Zivkov et al. 2018) and T66_G7 (containing 30 Dor; Tatton et al. 2013), all standing out for their higher $-\ln \mathcal{L}$ in Fig. 6. Substantial (and very time-consuming) changes in the analysis are planned to improve the model fitting in these regions of the LMC disc.

In addition, visual inspection of Fig. 9 suggests that there are a few *entire tiles* with deviant values of A_V. An example is tile 7_7 in the JK_s extinction map, for which A_V values are about ∼0.2 mag higher than in neighbouring tiles. These cases likely represent either degraded observing conditions or non-detected errors in the zero-points of a tile.

Considering the above-mentioned problems, our extinction maps are less detailed than many other extinction maps derived for the LMC. However, we note that our high-extinction regions coincide with those derived by many different authors using completely independent data and methods (see for instance Zaritsky et al. 2004; Furuta et al. 2019).

4.5 Distance maps

Similarly to extinction, we explore shifts in magnitude K_s that can be interpreted as distance variations across the LMC. True distance moduli can be computed with

$$\mu_0 = 18.50 + E(K_s) - A_{K_s} \quad (9)$$

from both the JK_s and YK_s cases. Results are plotted in Fig. 11.

Errors in μ_0 come from the 68 per cent confidence intervals indicated by the MCMC results, plus a minimum 0.02 mag error added in quadrature to take into account the grid effect in the Δm values (similarly to Section 4.4). Therefore, these maps incorporate the already-mentioned issues in the extinction maps, but fortunately enough this is a minor problem in the K_s band. Despite the negative extinctions values derived from the YK_s data, the true distance moduli obtained from the YK_s and JK_s cases have similar values, with a weighted least-squares fit indicating a systematic shift of just 0.03 mag between them. Much more worrying, instead, are the irregularities, on a tile-to-tile basis, present in the distance maps.

Anyway, a clear picture results from these distance maps: south-western LMC regions are systematically farther away than north-eastern regions. This is in agreement with all literature to date, and will be explored further in Section 5.1 below.

4.6 Metallicity shifts

Near-infrared photometry is in general less sensitive to metallicity than optical photometry, especially when distance modulus and extinction are considered as free adjustable parameters, as in our case. Anyway there is some dependency on metallicity encoded in VMC data, coming from subtle changes in the mean slope of the RGB, in the position and shape of the RC, and in the mean colour (compared to the RGB) and slope of the MS. This information is partially recovered by our MCMC code, in the form of the metallicity shifts with respect to the initially assumed AMR from Carrera et al. (2008), (Δ[Fe/H]$_1$, Δ[Fe/H]$_2$), at both very young and very old ages.

The resulting metallicity shifts present a lot of scatter, and no evidence of large-scale metallicity gradients in the LMC region presently explored. However, they clearly indicate that young LMC populations are better represented by metallicities slightly lower than those in the reference AMR from Carrera et al. (2008). Median values for the (Δ[Fe/H]$_1$, Δ[Fe/H]$_2$) coefficients are (− 0.084, 0.049) dex for the YK_s data, and (− 0.092, 0.004) dex for the JK_s data. Work is ongoing (Choudhury et al., in preparation) to explore the LMC metallicity trends from VMC data in a more systematic way.

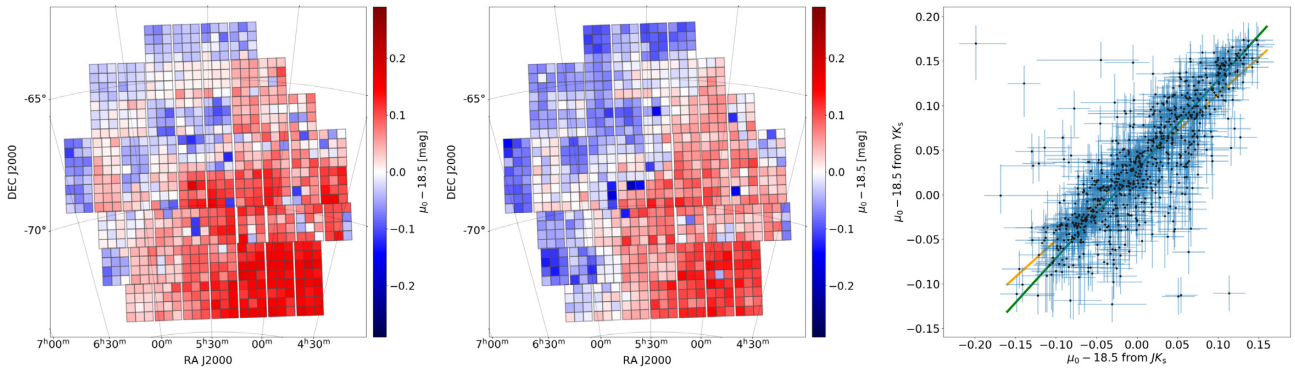

Figure 11. From left to right, we have the true distance moduli maps derived from YK_s and JK_s, and their relationship (as in Fig. 9). The two fitted relations are: a systematic shift of $\mu_0^{YK_s} = \mu_0^{JK_s} + 0.03$ mag (green), or a best-fitting line of $\mu_0^{YK_s} - 18.5 = 0.82\,(\mu_0^{JK_s} - 18.5) + 0.03$ mag (orange).

Table 3. Results for the fitting of the LMC plane using the distances to many subregions.

Case	$\alpha_{c,\,J2000}$ (deg)	$\delta_{c,\,J2000}$ (deg)	i (deg)	θ_0 (deg)	R_0 (kpc)[1]	Comments
van der Marel & Cioni (2001)[2]	82.25	−69.50	34.7 ± 6.2	122.5 ± 8.3	–	AGB stars
Olsen & Salyk (2002)	79.91	−69.45	35.8 ± 2.4	145 ± 4	–	optical red clump
Nikolaev et al. (2004)	79.40	−69.03	30.7 ± 1.1	151.0 ± 2.4	–	Cepheids
Koerwer (2009)	80.89	−69.75	23.5 ± 0.4	154.6 ± 1.2	–	NIR red clump
Rubele et al. (2012)	79.40	−69.03	26.2 ± 2.0	129.1 ± 13.0	–	fit of early VMC data
Subramanian & Subramaniam (2013)	79.91	−69.45	25.7 ± 1.6	141.5 ± 4.1	–	NIR red clump
Deb et al. (2018)	80.78	−69.03	25.110 ± 0.365	154.702 ± 1.378	–	multi-λ Cepheids
Choi et al. (2018)	82.25	−69.5	$25.86^{+0.73}_{-1.39}$	$149.23^{+6.43}_{-8.35}$	–	optical red clump
This work, all YK_s	79.40	−69.03	23.99 ± 0.33	$141.40^{+0.98}_{-0.96}$	51.21 ± 0.02	
This work, YK_s filtered	79.40	−69.03	24.38 ± 0.34	$141.19^{0.96}_{-0.94}$	51.15 ± 0.02	
This work, all JK_s	79.40	−69.03	24.06 ± 0.34	$149.52^{0.93}_{-0.94}$	50.58 ± 0.02	
This work, JK_s filtered	79.40	−69.03	23.92 ± 0.34	$149.41^{+0.95}_{-0.93}$	50.51 ± 0.02	

Note. [1] R_0 are the heliocentric distances to the LMC centre. We omit the values assumed/derived by other authors, since they rely on very different (and sometimes outdated) distance calibrations. [2] This is the plane assumed by HZ09 (see Section 5.2).

5 DISCUSSION

Now that we have large-scale maps of SFR(t) with different degrees of reliability across the LMC disc, and additional information about large-scale changes in properties such as extinction and distance, we discuss ways in which we can better interpret and improve these results, while still adopting the present data, models, and algorithms.

5.1 The LMC geometry

A first-order description of the LMC geometry is that the young and intermediate-age populations are on an inclined thin disc, as suggested by distance indicators such as Cepheids (e.g. Nikolaev et al. 2004) and RC stars (e.g. Olsen & Salyk 2002), while the very old populations have a thicker and more spheroidal distribution, as indicated by the RR Lyrae (e.g. Subramaniam 2006). Assuming that our method is efficiently measuring the mean distance of every subregion, we can fit an inclined disc to our sets of true distance moduli, similarly to what was done by the above-mentioned authors, and updating a similar fit which was done by Rubele et al. (2012) using just four tiles of VMC data. To fit the plane, we proceed as follows:

(i) We fix the coordinates of the LMC centre, (α_c, δ_c), adopting one of the several possible choices in the literature (see Table 3).

(ii) Every subregion is located in Cartesian space by using its central coordinates and the median value of μ_0 determined from our fit (equation 9), together with its error.

(iii) The best-fitting plane is determined by looking for the heliocentric distance to the LMC centre, R_0, the disc inclination on the plane of the sky, i (where $i = 0°$ means a face-on disc), and the position angle of the line of nodes, θ_0, that minimizes the distance residuals to the plane.

(iv) The initial guess of (R_0, i, θ_0) is taken from literature values, and it is let to evolve via the MCMC code *emcee* (Foreman-Mackey et al. 2013).

To limit the discussion to the most reliable subregions, we also apply the following cuts to the set of subregions:

(i) K_s(75 per cent completeness) > 18.5 mag
(ii) $-\ln \mathcal{L} < 6000$

They eliminate the central LMC from the fit, including a large fraction of its Bar (see Fig. 12).

Results are presented in Table 3, where we also compare them with a series of similar determinations, all based on fitting a plane to the distances of indicators distributed across the LMC disc. Discussing these results in detail is beyond the scope of this paper. We just notice that the plane we fit is in better agreement with previous determinations based on the NIR magnitude of the RC (Koerwer

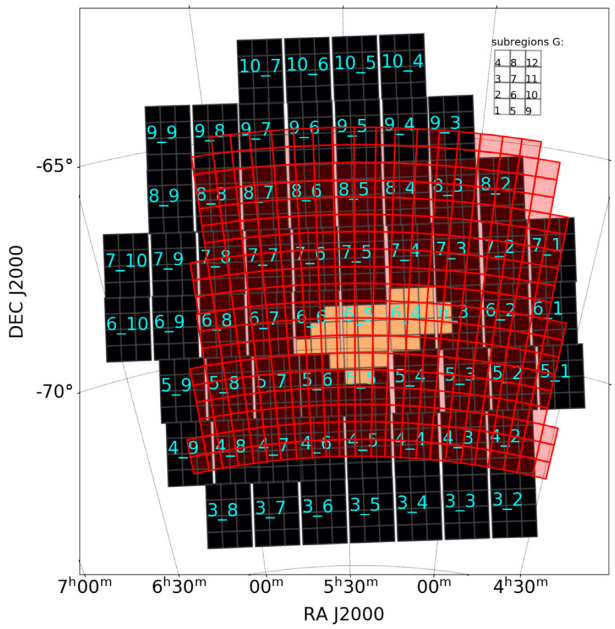

Figure 12. Comparison between the sky areas covered by our SFH maps (dark and yellow areas) and those of HZ09 (red/pink areas). The yellow areas are those more affected by crowding (K_s(75 per centcompleteness) < 18.5 mag), which are excluded from some of our comparisons.

2009; Subramanian & Subramaniam 2013), than on determinations based on Cepheids, or on optical data. This is not surprising because the $E(K_s)$ values we derive (and hence the μ_0 from equation 9) are strongly constrained by the K_s magnitude of the RC in VMC data. Our results, however, differ from determinations based *only* on the RC magnitude, because (1) we consider stars in many other evolutionary stages in the fitting, and (2) we naturally take into account the intrinsic variations in the RC absolute magnitude as a function of population age and metallicity (see Girardi 2016).

Our best results are illustrated in Fig. 13. This fitted plane is expected to provide a first-order correction to the distance of all LMC stars.

5.2 Spatial comparison with the HZ09 SFR(t)

As already mentioned, the most comprehensive study of the SFH across the LMC so far is from HZ09, performed for an 8.5° × 7.5° area of the optical MCPS survey. That study samples the same age range as VMC. Their survey area was divided in cells 24 arcmin × 24 arcmin large, or one-fourth of that size for the innermost LMC regions. The total area explored by HZ09 is compared to ours in Fig. 12.

By comparing our SFH maps of Figs 5 and B1, with those in fig. 8 of HZ09, it is clear that both works present some similar features, especially at young ages. To allow a quantitative comparison with our results, we resample the SFH maps from HZ09 for the same areas of our subregions. It means that for every subregion, we find all the spatial cells defined by HZ09 that intersect it, and add the fraction of HZ09's SFR(t) corresponding to the intersecting area.

Representative comparisons between the derived SFR(t) are shown in Figs 14 and 15, for two sections of tiles uniformly covered in both works – namely the northernmost section of tile LMC 4_3, and the southernmost section of tile LMC 8_6. We use the same plotting approach of HZ09, who simply connect their values of log (t/yr) with values of inferred SFR(t). Although their SFR(t) values actually apply to log (t/yr) intervals 0.2 or 0.3 dex wide (and not to a single point in age), it is not clear exactly where these age intervals start and finish. This makes the quantitative comparison somewhat uncertain.

The results of these comparisons vary a lot, going from the 'excellent agreement' apparent for a few subregions, to surprising differences even for the very young SFR(t), which should have been well sampled by both VMC and MCPS. In the case of tile LMC 4_3 (Fig. 14), the agreement appears quite good for all ages older than 1 Gyr: there was a strong peak of SFR(t) for ages between 2 and 4 Gyr ($9.3 < \log(t/\mathrm{yr}) < 9.6$), preceded by much smaller values of SFR(t) at older ages. At younger ages, there seems to be a discrepancy at ages of $\log(t/\mathrm{yr}) \simeq 8.6$, in which HZ09 suggest a peak of SFR(t), at least in the southern part of the tile, which is absent from our maps. At even younger ages, for most of the subregions we only have upper limits to the SFR(t), but these upper limits are much smaller than the upper limits found by HZ09. We identify an episode of enhanced SFR(t) at ages $8.1 < \log(t/\mathrm{yr}) < 8.4$ yr at the top (northern) part of this tile, which has a counterpart in the 10^8 yr peak shown by HZ09 maps. Fig. 14 also illustrates that, at least for this tile, the SFR(t) obtained from YK_s and JK_s data sets are about the same.

The tile LMC 8_6 covers a good fraction of the star-forming region known as Constellation III. There are striking similarities with the SFR(t) derived by HZ09 at all intermediate and old ages – with the absolute values of SFR(t) differing by less than expected from their 68 per cent confidence intervals (Fig. 15). At ages around 10^8 yr, however, HZ09 maps tend to present stronger peaks of SFR than our maps suggest. At the even younger ages of $\log(t/\mathrm{yr}) < 7.2$, our maps capture the presence of bursts of SFR(t) in the same places as HZ09, but with a somewhat reduced intensity, and only in the JK_s-derived maps.

The quantitative comparison between our SFR(t) and the HZ09 one is more complicated than suggested in these figures, because of a series of significant differences in the analyses. A fundamental one is in the IMFs used to model the single-burst stellar populations: a normalized Kroupa (2001) in our case, Salpeter (1955) in the case of HZ09. Different IMFs imply that the multiplicative constants that are used to convert the numbers of observed (and fitted) stars into a total initial mass of a stellar population – and hence into a given SFR(t) in units of $\mathrm{M_\odot yr^{-1}}$ – should have been different. None the less, the final results for the SFR(t) appear on a comparable scale in Figs 14 and 15, *suggesting* that HZ09 normalized their IMF in a way similar to us. Unfortunately, details of this IMF normalization are not specified in their work.

There are many other differences between our derivation of the SFR(t), and those by HZ09, among which our metallicity distribution is constrained around a reference AMR, while in HZ09 the metallicities can simultaneously occupy four different values at every age; we fit the mean values of extinction and distance independently for every subregion, whereas HZ09 apply pre-defined corrections to these parameters; our studies use different generations of stellar models and methods to find the best solutions; over the Bar, HZ09 fix the shape of their old SFR(t), for $t > 4$ Gyr, so as to replicate the results obtained by other authors using deeper *HST* observations, while we use *only* VMC data to derive all quantities. The most notable difference, however, is that HZ09 use optical data, while we use the near-infrared. Optical data may provide a better colour separation for young populations, but on the other hand they are more affected by interstellar extinction and its dispersion inside the young LMC disc. Therefore, the advantage of using either one of these data sets is not obvious. It is noteworthy and reassuring that, despite all these differences, the resulting SFR(t) do not appear dramatically different,

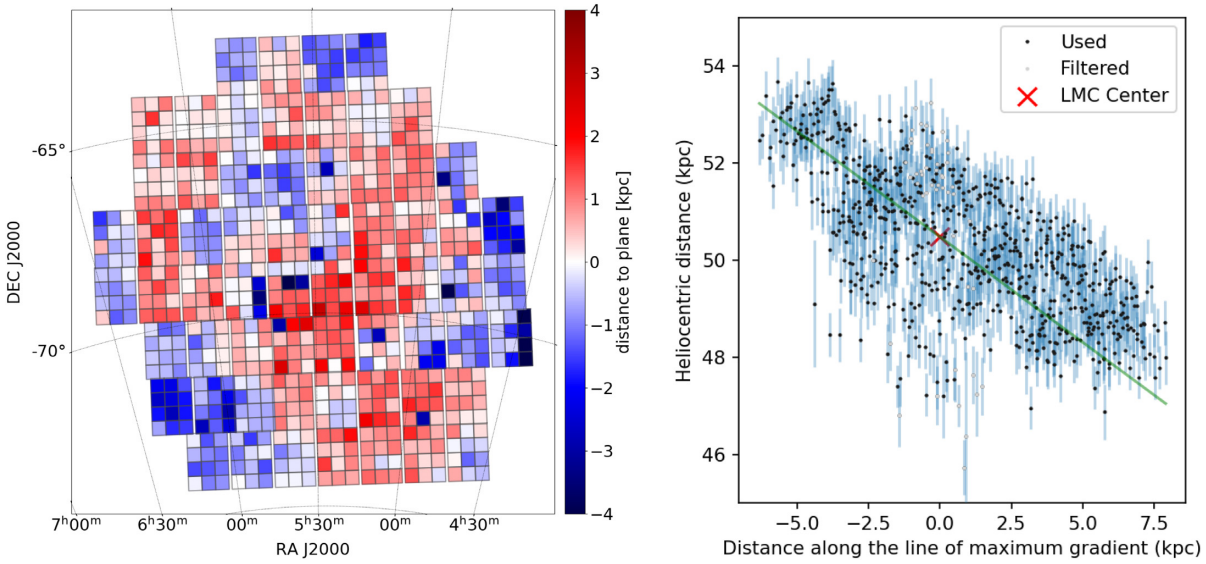

Figure 13. Left-hand panel: residuals from the fitting of the LMC plane using the most reliable regions and JK_s photometry. Right-hand panel: heliocentric distance versus distance along the line of maximum gradient for this same fit.

at least not for the $t > 10^8$ yr ages that contain most of the stellar mass formed in the LMC.

5.3 The problem at very young ages

A surprising result from this comparison is that our SFH maps from YK_s data seem to underestimate the SFR(t) for the two youngest age bins, $6.6 < \log(t/\mathrm{yr}) < 6.9$ and $6.9 < \log(t/\mathrm{yr}) < 7.2$, compared to both the JK_s-derived maps and the HZ09 results. We verify that at these very young ages all the evolved stars happen to be located above the magnitude cut of $K_s < 12$ mag. As a consequence, the only information that is actually used to constrain the SFR(t) for these young age bins are the (very small) star counts along the upper main sequence, and especially those located at colours close to zero in the $12 < K_s < 14$ mag interval. For all older ages, instead, the red core helium-burning stars enter decisively in the Hess diagrams being analysed. While this fact does not explain the differences between the YK_s and JK_s results, they actually warn us that the SFR(t) at $\log(t/\mathrm{yr}) < 7.2$ might be significantly less reliable than the results for all older ages.

Very young star formation is often associated with higher extinction (i.e. larger than the one measured for older populations in the same area) and/or larger extinction dispersion. These effects are still not considered in our models, and could be contributing to these systematic errors.

5.4 Comparison with the HZ09 SFR(t) for a large area

The left-hand panel in Fig. 16 presents a comparison between the two SFR(t) integrated over a large area (57.42 deg^2) where we have results from both VMC and MCPS. Keeping in mind all the above-mentioned differences in the data and analyses, one thing is apparent: The two SFR(t) are comparable for ages above 10^8 yr, while at younger ages HZ09 tend to present larger values of SFR(t) – about two to three times larger than ours, although this difference is comparable with the large uncertainties that characterize results for very young populations. It is also apparent that there is a significant difference between our results for YK_s and JK_s at very young ages, with the YK_s tending to miss the very young bursts that instead are detected with the JK_s data, and also by HZ09. The reason for this behaviour is not clear, but might be due to the stronger differential reddening that generally affects these regions with very young bursts.

At intermediate ages, the most notable difference is that our results point to a peak of SFR(t) in the $\log(t/\mathrm{yr})$ interval between 8.8 and 9.0, which is absent from the HZ09 results. However, this difference is almost completely due to subregions in the LMC Bar, which are more affected by crowding, and which are analysed differently in the HZ09 case (with their partial use of results from *HST* for ages older than 4 Gyr). Indeed, the right-hand panel of Fig. 16 presents the same comparison limited to all areas with K_s(75 per centcompleteness) > 18.5 mag, hence excluding about 4.5 deg^2 over the LMC Bar. As can be seen, the peak at the 8.8–9.0 $\log(t/\mathrm{yr})$ interval almost disappears from our SFR(t), and a better agreement with HZ09 is reached in this case.

5.5 The total mass of stars ever formed

The left-hand panel of Fig. 17 presents the total SFR(t) integrated over the entire area analysed in this work. The main features in this plot were already commented in comparison with similar features derived from HZ09. One aspect clearer in this figure, however, is the large uncertainties about the confidence levels in the total SFR(t). If we assume that the 756 subregions analysed provide independent solutions for their SFR(t), then errors should be combined in quadrature, with the consequence that the total SFR(t) presents extremely narrow confidence regions. In this case, the YK_s and JK_s results are generally in disagreement. If instead we consider errors as mostly systematic, and simply add the confidence intervals region by region, we obtain final errors in the total SFR(t) which are much larger, and which generally allow for 'agreement' between YK_s and JK_s results. The correct alternative is likely somewhere in between these two cases.

The total SFR(t) can be integrated from the epoch of LMC formation at $\log(t/\mathrm{yr}) = 10.2$, to derive the total mass in stars formed as a function of time, which is depicted in the right-hand panel of

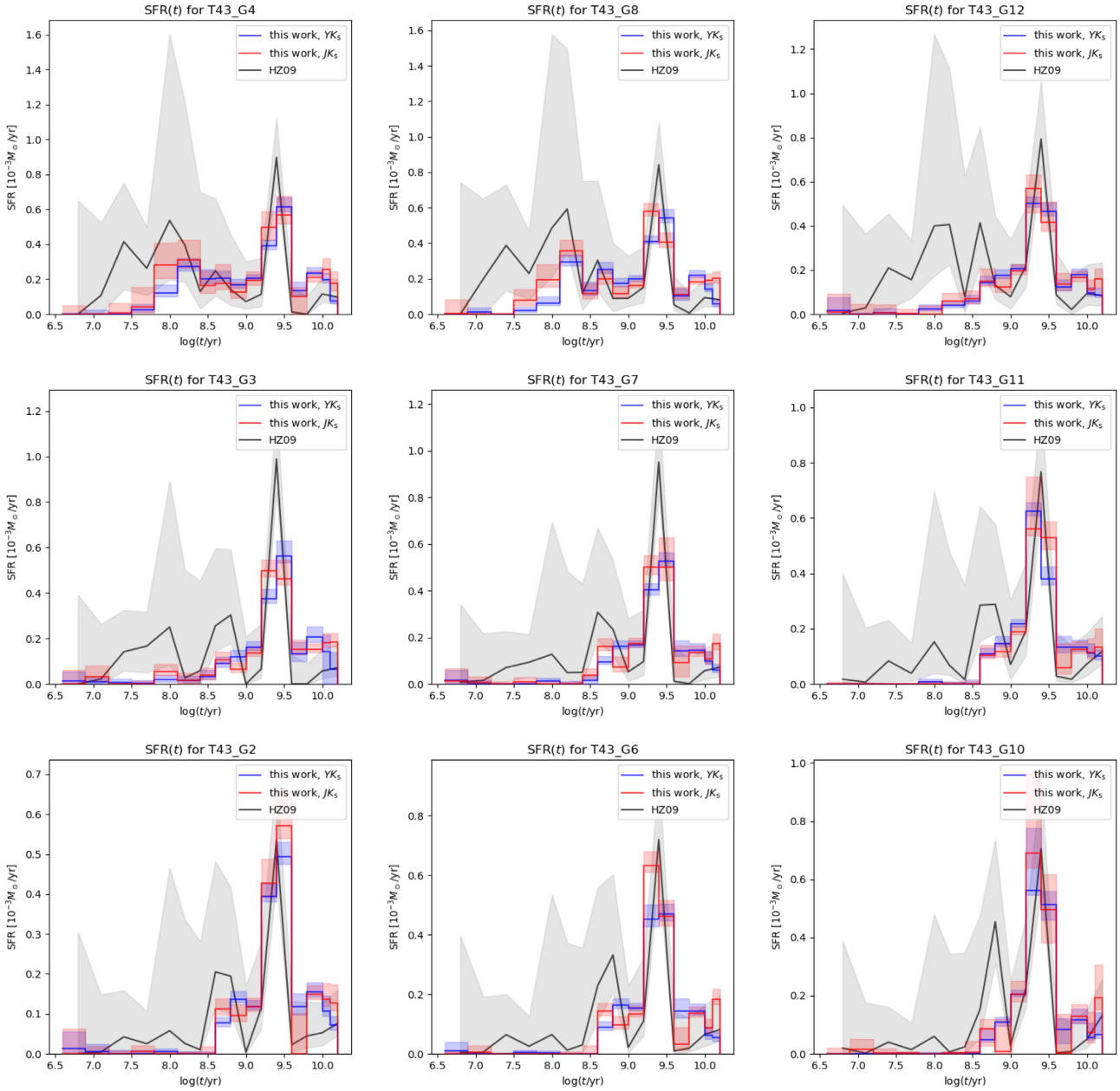

Figure 14. Comparison between our SFR(t) and those of Harris & Zaritsky (2009), for subregions covering the northern three-fourths of the tile LMC 4_3. They are plotted in the same way as they appear in the sky, with northermost subregions at the top and westernmost subregions to the right. The different curves illustrate our derived SFR(t), and the HZ09 SFR(t) resampled for the same area. The full lines correspond to the median values of the SFR(t), while the shaded areas correspond to the 68 per cent confidence intervals.

Fig. 17. The total mass of stars ever formed is $\sim 2.5 \times 10^9$ $M_\odot$. If we adopt just the random errors, the mass uncertainty is of about 20 per cent. However, the real uncertainties are likely much larger than that.

A total mass of $\sim 2.5 \times 10^9$ $M_\odot$ is consistent with the 2.2×10^9 $M_\odot$ value derived by HZ09 (see their fig. 14). It is worth remarking that a substantial fraction of this formed mass (about a third) has since been either lost to the interstellar medium or locked into compact stellar remnants. On the other hand, the most recent star formation in the LMC takes place from mass partly recycled from previous generations. Therefore, the total mass of $\sim 2.5 \times 10^9$ $M_\odot$ gives only an order-of-magnitude estimate for the stellar mass that should be present now in the LMC.

5.6 Preliminary indications for dynamical models of the Magellanic System

As already mentioned, the present maps might be a useful resource to constrain the past history of the Magellanic System via their hydrodynamical simulations. This topic is well beyond the scope of this paper. However, looking at our results, and at the comparison with previous SFH maps from HZ09, two aspects appear more relevant and worth of attention:

(i) Our maps show a remarkably clear spatially resolved SFR(t) for all ages between a few tens of Myr and $\sim$2 Gyr. Previous simulations of the LMC–SMC interaction demonstrated the last strong LMC–SMC interaction occurred about 0.1–0.2 Gyr ago, possibly triggering

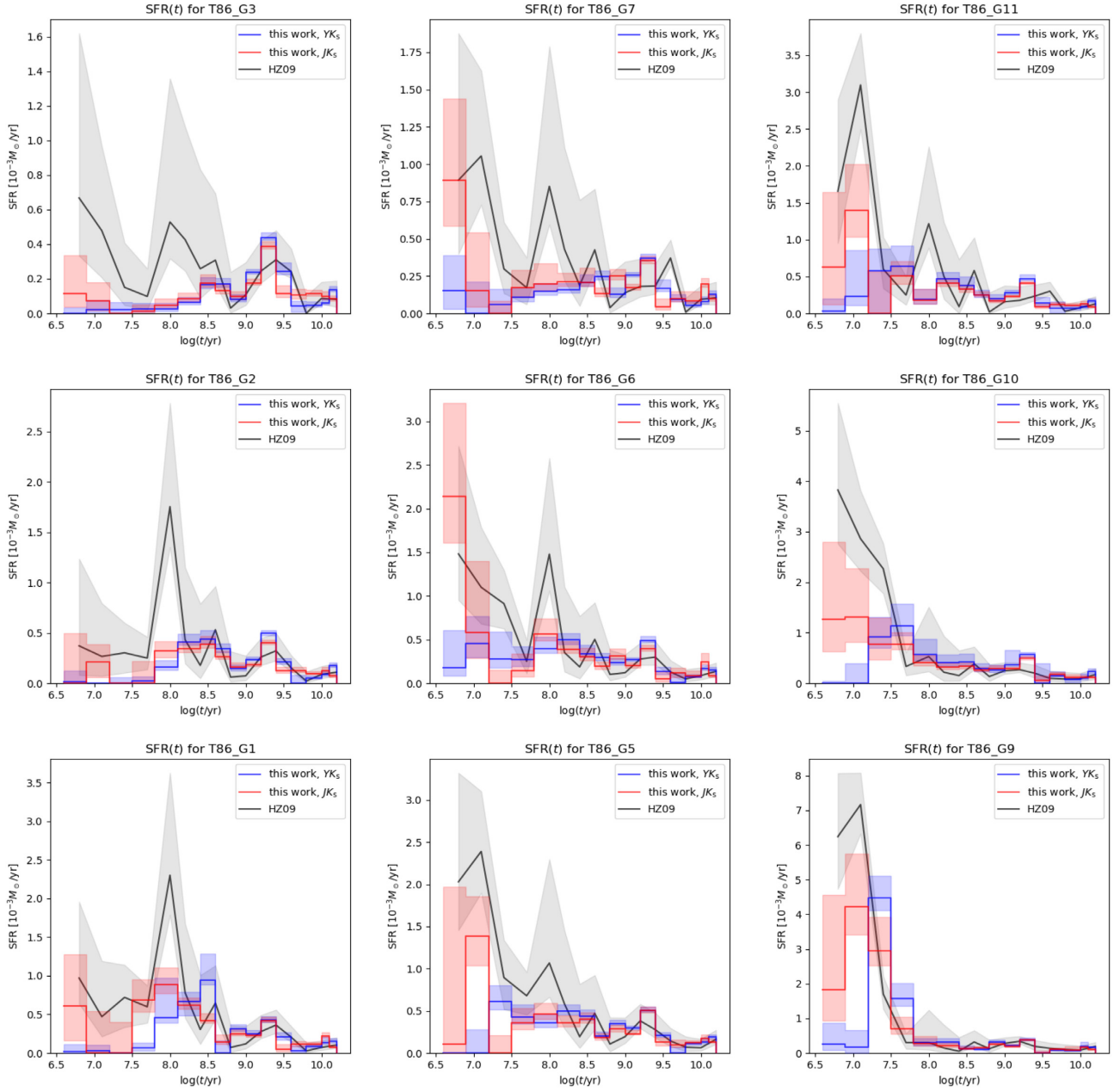

Figure 15. The same as Fig. 14 but for the southern section of the tile LMC 8_6, covering part of the star forming area known as Constellation III.

massive star formation in the Clouds (e.g. Yoshizawa & Noguchi 2003). However, they did not predict the detailed distributions of the young stellar populations of the LMC formed by such intense interaction. The locations of the VMC tiles with SFR(t) peaking at 0.1–0.2 Gyr can thus provide strong constraints on the LMC–SMC interaction history over the last 0.2 Gyr. We note that the more interesting age interval corresponds to our age bin $i = 6$, which presents a bar and at least one clear spiral arm in Figs 5 and B1.

(ii) The LMC bar is very well defined in the SFR(t) maps, being slim at all ages until ∼1 Gyr, and still clearly present until ∼1.6 Gyr (Figs 5 and B1). Although previous simulations showed the formation of a stellar bar in the LMC, in these simulations both old and new stars show strong bar-like distributions (Bekki & Chiba 2005). The observed lack of a strong bar in older populations – if confirmed in maps less affected by crowding than ours – would suggest that the LMC already had a dynamically hot thick disc *before* the formation of the thin stellar bar (see e.g. Bekki 2009).

6 CONCLUSIONS

In this work, we provide large-scale maps of the spatially resolved SFH for the LMC galaxy. The main highlights of this work are:

(i) We cover an area of 96 deg^2, superseding the large area previously covered by HZ09 maps.

(ii) We perform a uniform analysis of the photometric data, separately for the YK_s and the JK_s data sets. The VMC data set is by itself very uniform, but for changes in observing conditions that appear as small tile-to-tile changes in the error functions and photometric zero-points. These changes were taken into account in the analysis.

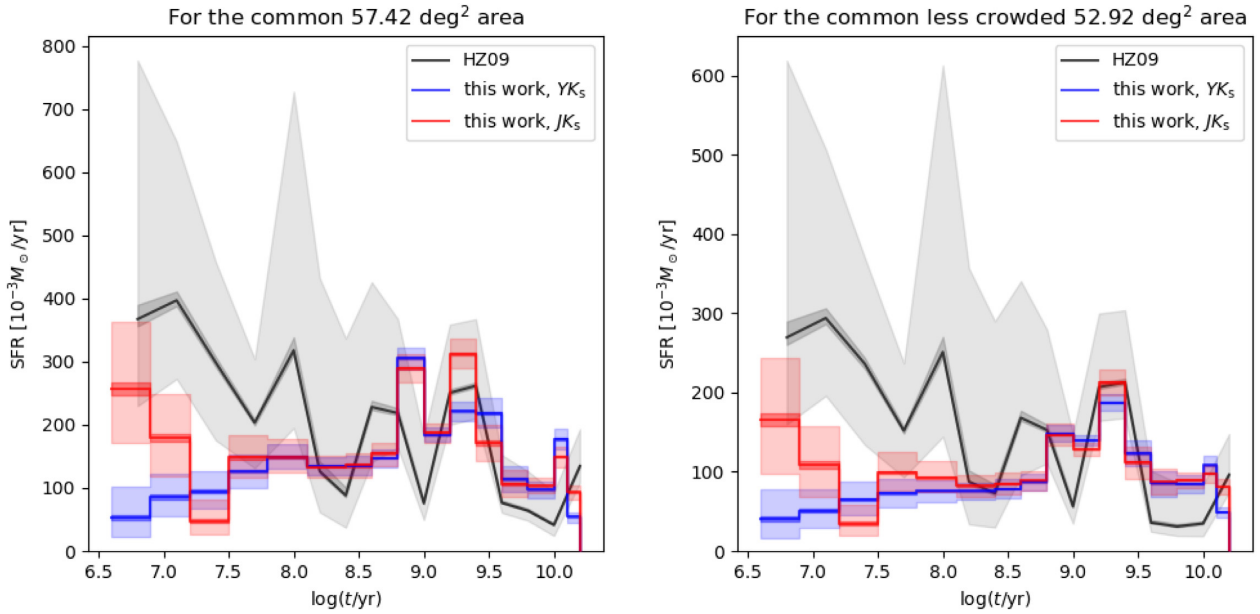

Figure 16. Comparison between our SFR(t) and those of Harris & Zaritsky (2009), integrated over many subregions. The left-hand panel includes the entire area in which we have results from both surveys, while in the right-hand panels we consider only the regions with K_s(75 per centcompleteness) > 18.5 mag. In the comparison, one should better exclude the two youngest age bins, for log(t/yr) < 7.2, which are considered to be significantly more uncertain than all the others.

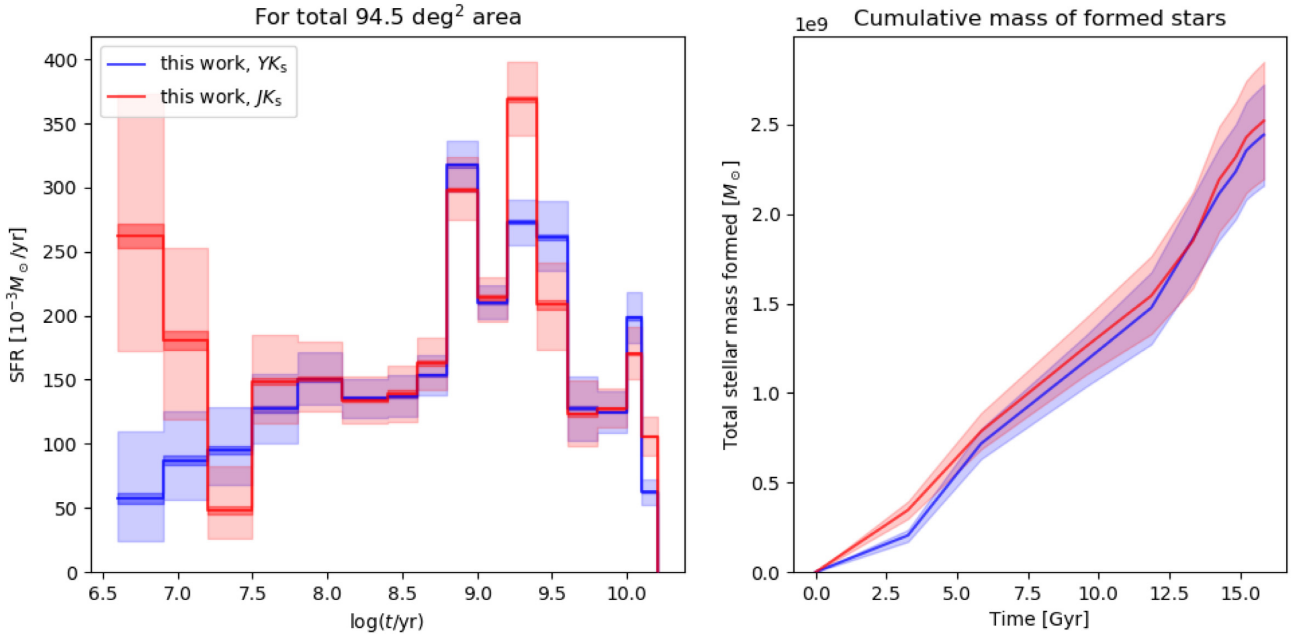

Figure 17. Left-hand panel: Total SFR(t) integrated over our total area, from both the YK_s and JK_s solutions (blue and red continuous lines, respectively). The shaded areas represent the errors (or confidence regions) computed with quite different approaches: either simply adding minimum/maximum intervals for all subregions, just as if all errors were systematic (light shaded areas), or adding errors in quadrature, as if all errors were random (strong shaded areas). The right-hand panel shows the cumulative mass of formed stars, obtained by integration of the SFR(t) since the epoch of galaxy formation at log(t/yr) = 10.2. In this case, the confidence regions reflect the random errors only.

(iii) Our results are generally consistent with previous works, but with some significant quantitative differences. We find a best-fitting plane for the LMC that generally agrees with those derived from near-infrared photometry of the red clump. Our SFR(t) are similar to those of HZ09, but for the trend of presenting smaller SFR(t) values at young ages.

(iv) The periods of most intense star formation in the LMC are at intermediate ages, roughly between 0.5 and 4 Gyr, in which the total star formation across the entire galaxy reaches values of about 0.3 $M_\odot yr^{-1}$. For the remaining epochs the total SFR(t) is typically half of this maximum value. Two peaks of enhanced SFR(t) appear in our maps, in the age intervals 8.8 < log(t/yr) < 9.0 (0.63 to 1 Gyr)

and $9.2 < \log(t/\mathrm{yr}) < 9.6$ (1.6 to 4 Gyr). Regions in the LMC Bar are the main responsible for the youngest of these peaks. Our results do not seem to contradict any of the general conclusions reached by HZ09, but they suggest corrections to the ages of periods of enhanced SFR(t), and to their quantitative values.

(v) The SFH maps are provided as a useful resource for modelling the present structure of the LMC, and its past history through chemo-dynamical evolutionary models of the LMC+SMC + MW system. Particularly interesting are the distributions of the stellar populations with ages 0.1–0.2 Gyr, which can be used to constrain the interaction histories of the LMC and the SMC, and the slim bar observed at ages younger than ∼1 Gyr, which can provide strong constrains on the dynamical properties of the LMC during/before its interaction with the SMC and the MW.

Our SFH results will be subsequently used in a series of works aimed at improving our knowledge of the Magellanic Clouds and their stars. Among these works, we will be reconsidering the recent calibration of TP-AGB evolutionary models by Pastorelli et al. (2020), who used a subsample of 72 LMC subregions comprising a total area of ∼9 deg^2. A first comparison of the present SFH with the preliminary solution used by Pastorelli et al. (2020) for these subregions reveals modest differences in the SFR(t), of magnitudes similar to the random errors. More systematic changes appear in the AMR, which is now constrained to lie close to the relation indicated by spectroscopic data. Anyhow the impact of the new SFH on the TP-AGB models is still not assessed, and will be the subject of a future study. We expect that a potential larger effect may result from the fact that the LMC area useful for the TP-AGB calibration – given by the intersection of the VMC survey area with the AGB catalogue classified by Boyer et al. (2011) – can now be increased by a factor of about 6. Such an increase in area results in a substantial improvement in the statistics and will also make it possible to calibrate the TP-AGB models in subregions characterized by very different mean ages, and hence different mean progenitor masses.

The analyses of the present data set represented a major effort in terms of processing of VMC data, and its fitting via a long process involving many different components derived from theoretical models. Simplifications were necessary to deal with the entire data set without running out of computer storage and CPU time. Some of these simplifications will be progressively abandoned in the near future, as we add more VMC tiles to our data base, and as we reanalyse present tiles in the search of better solutions. In particular, we are currently planning to perform more ASTs so as to include fainter sections of the Hess diagrams, to include 2MASS data in JK_s passbands to better probe the very young SFR(t), to split the data in smaller subregions so as to better deal with variable extinction in central parts of the LMC, and to separate all known star clusters from the field. Moreover, we can also implement improvements in the fitting process itself, starting from the initial solutions derived for this paper: It is somewhat evident that we can aim at a better description of the spatial distribution of stars and dust inside every subregion, also adopting constraints from neighbouring subregions. On the other hand, the new accuracy standards set by Gaia parallaxes (Gaia Collaboration 2018, 2021a) and by asteroseismology (Khan et al. 2018; Mackereth et al. 2021), and the realization of the importance of fast-rotating stars (Costa et al. 2019), are prompting further revision of our stellar models, which will have its implications for evolutionary models of LMC stars. For all these reasons, we plan to reanalyse the entire VMC data set of 104.8 deg^2 across the LMC in less than 2 yr time.

ACKNOWLEDGEMENTS

Many of us acknowledge the support from the ERC Consolidator Grant funding scheme (project STARKEY, grant agreement n. 615604). M-RC and CPMB acknowledge support the European Research Council (ERC) under the European Unions' Horizon 2020 research and innovation programme (grant agreement no. 682115). This work is based on the observations collected at the European Organisation for Astronomical Research in the Southern Hemisphere under ESO programme 179.B-2003. We thank the CASU and the WFAU for providing calibrated data products under the support of the Science and Technology Facility Council (STFC) in the UK.

DATA AVAILABILITY

The image data used in this paper are available in the VISTA Science Archive (VSA), at http://horus.roe.ac.uk/vsa. The PSF photometry and ASTs will be soon shared by ESO in the regular VMC data releases (http://www.eso.org/rm/publicAccess#/dataReleases).

REFERENCES

Badenes C., Maoz D., Ciardullo R., 2015, ApJ, 804, L25
Bekki K., 2009, MNRAS, 393, L60
Bekki K., Chiba M., 2005, MNRAS, 356, 680
Boyer M. L. et al., 2011, AJ, 142, 103
Bressan A., Marigo P., Girardi L., Salasnich B., Dal Cero C., Rubele S., Nanni A., 2012, MNRAS, 427, 127
Cardelli J. A., Clayton G. C., Mathis J. S., 1989, ApJ, 345, 245
Carrera R., Gallart C., Aparicio A., Hardy E., 2011, AJ, 142, 61
Carrera R., Gallart C., Hardy E., Aparicio A., Zinn R., 2008, AJ, 135, 836
Castelli F., Kurucz R. L., 2003, in Piskunov N., Weiss W. W., Gray D. F., eds, Proc. IAU Symp. 210, Modelling of Stellar Atmospheres. Kluwer, Dordrecht, p. A20
Chen Y. et al., 2019, A&A, 632, A105
Chen Y., Bressan A., Girardi L., Marigo P., Kong X., Lanza A., 2015, MNRAS, 452, 1068
Chen Y., Girardi L., Bressan A., Marigo P., Barbieri M., Kong X., 2014, MNRAS, 444, 2525
Choi Y. et al., 2018, ApJ, 866, 90
Cioni M. R. L. et al., 2011, A&A, 527, A116
Costa G., Girardi L., Bressan A., Chen Y., Goudfrooij P., Marigo P., Rodrigues T. S., Lanza A., 2019, A&A, 631, A128
Cross N. J. G. et al., 2012, A&A, 548, A119
Cusano F. et al., 2021, MNRAS, 504, 1
Dal Tio P., et al., 2021, MNRAS, 506, 5681
Dalton G. B., Sutherland W. J., Emerson J. P., Woodhouse G. F. W., Terrett D. L., Whalley M. S., 2010, in McLean I. S., Ramsay S. K., Takami H., eds, Proc. SPIE Conf. Ser. Vol. 7735, Ground-based and Airborne Instrumentation for Astronomy III. SPIE, Bellingham, p. 77351J
Deb S., Ngeow C.-C., Kanbur S. M., Singh H. P., Wysocki D., Kumar S., 2018, MNRAS, 478, 2526
Dolphin A. E., 2002, MNRAS, 332, 91
Emerson J., McPherson A., Sutherland W., 2006, The Messenger, 126, 41
Foreman-Mackey D., Hogg D. W., Lang D., Goodman J., 2013, PASP, 125, 306
Freedman W. L. et al., 2001, ApJ, 553, 47
Furuta T., Kaneda H., Kokusho T., Ishihara D., Nakajima Y., Fukui Y., Tsuge K., 2019, PASJ, 71, 95
Gaia Collaboration, 2018, A&A, 616, A10
Gaia Collaboration, 2021a, A&A, 649, A1
Gaia Collaboration, 2021b, A&A, 649, A7
Gallart C., Stetson P. B., Meschin I. P., Pont F., Hardy E., 2008, ApJ, 682, L89
Girardi L. et al., 2008, PASP, 120, 583
Girardi L., 2016, ARA&A, 54, 95

Girardi L., Groenewegen M. A. T., Hatziminaoglou E., da Costa L., 2005, A&A, 436, 895
González-Fernández C. et al., 2018, MNRAS, 474, 5459
Groenewegen M. A. T. et al., 2019, A&A, 622, A63
Harris J., Zaritsky D., 2001, ApJS, 136, 25
Harris J., Zaritsky D., 2009, AJ, 138, 1243
Hogg D. W., Foreman-Mackey D., 2018, ApJS, 236, 11
Husser T.-O., Wende-von Berg S., Dreizler S., Homeier D., Reiners A., Barman T., Hauschildt P. H., 2013, A&A, 553, A6
Indebetouw R. et al., 2005, ApJ, 619, 931
Kallivayalil N., van der Marel R. P., Besla G., Anderson J., Alcock C., 2013, ApJ, 764, 161
Kerber L. O., Girardi L., Rubele S., Cioni M. R., 2009, A&A, 499, 697
Khan S., Hall O. J., Miglio A., Davies G. R., Mosser B., Girardi L., Montalbán J., 2018, ApJ, 859, 156
Koerwer J. F., 2009, AJ, 138, 1
Kroupa P., 2001, MNRAS, 322, 231
Kroupa P., Weidner C., Pflamm-Altenburg J., Thies I., Dabringhausen J., Marks M., Maschberger T., 2013, The Stellar and Sub-Stellar Initial Mass Function of Simple and Composite Populations. Springer, p. 115
Lebzelter T., Mowlavi N., Marigo P., Pastorelli G., Trabucchi M., Wood P. R., Lecoeur-Taïbi I., 2018, A&A, 616, L13
Mackereth J. T. et al., 2021, MNRAS, 502, 1947
Maoz D., Badenes C., 2010, MNRAS, 407, 1314
Meschin I., Gallart C., Aparicio A., Hidalgo S. L., Monelli M., Stetson P. B., Carrera R., 2014, MNRAS, 438, 1067
Metropolis N., Rosenbluth A. W., Rosenbluth M. N., Teller A. H., Teller E., 1953, J. Chem. Phys., 21, 1087
Miglio A. et al., 2012, MNRAS, 419, 2077
Monteagudo L., Gallart C., Monelli M., Bernard E. J., Stetson P. B., 2018, MNRAS, 473, L16
Nidever D. L. et al., 2017, AJ, 154, 199
Nidever D. L. et al., 2021, AJ, 161, 74
Nikolaev S., Drake A. J., Keller S. C., Cook K. H., Dalal N., Griest K., Welch D. L., Kanbur S. M., 2004, ApJ, 601, 260
Olsen K. A. G., Salyk C., 2002, AJ, 124, 2045
Pastorelli G. et al., 2019, MNRAS, 485, 5666
Pastorelli G. et al., 2020, MNRAS, 498, 3283
Pieres A. et al., 2020, MNRAS, 497, 1547
Pietrzyński G. et al., 2009, ApJ, 697, 862
Pietrzyński G. et al., 2019, Nature, 567, 200
Press W. H., Teukolsky S. A., Vetterling W. T., Flannery B. P., 1992, Numerical Recipes in C: The Art of Scientific Computing. Cambridge: University Press, Cambridge, UK
Reimers D., 1975, Mem. Soc. R. Sci. Liege, 8, 369
Rubele S. et al., 2012, A&A, 537, A106
Rubele S. et al., 2015, MNRAS, 449, 639
Rubele S. et al., 2018, MNRAS, 478, 5017
Salpeter E. E., 1955, ApJ, 121, 161
Sarbadhicary S. K. et al., 2021, ApJ, 912, 140
Schlafly E. F. et al., 2016, ApJ, 821, 78
Skrutskie M. F. et al., 2006, AJ, 131, 1163
Sollima A., Beccari G., Ferraro F. R., Fusi Pecci F., Sarajedini A., 2007, MNRAS, 380, 781
Subramaniam A., 2006, A&A, 449, 101
Subramaniam A., Subramanian S., 2010, in Ojha D. K., ed., Interstellar Matter and Star Formation: A Multi-wavelength Perspective, Astronomical Society of India Conference Series. p. 107
Subramanian S., Subramaniam A., 2013, A&A, 552, A144
Tatton B. L. et al., 2013, A&A, 554, A33
Trabucchi M., Wood P. R., Montalbán J., Marigo P., Pastorelli G., Girardi L., 2019, MNRAS, 482, 929
Trabucchi M., Wood P. R., Mowlavi N., Pastorelli G., Marigo P., Girardi L., Lebzelter T., 2021, MNRAS, 500, 1575
van der Marel R. P., Cioni M.-R. L., 2001, AJ, 122, 1807
Vanhollebeke E., Groenewegen M. A. T., Girardi L., 2009, A&A, 498, 95
Wang S., Jiang B. W., 2014, ApJ, 788, L12
Weisz D. R., Dolphin A. E., Skillman E. D., Holtzman J., Dalcanton J. J., Cole A. A., Neary K., 2013, MNRAS, 431, 364
Williamson D., Martel H., 2021, ApJ, 907, 9
Yoshizawa A. M., Noguchi M., 2003, MNRAS, 339, 1135
Zaritsky D., Harris J., Thompson I. B., Grebel E. K., 2004, AJ, 128, 1606
Zasowski G. et al., 2009, ApJ, 707, 510
Zivkov V. et al., 2018, A&A, 620, A143

SUPPORTING INFORMATION

Supplementary data are available at *MNRAS* online.

suppl_data

Please note: Oxford University Press is not responsible for the content or functionality of any supporting materials supplied by the authors. Any queries (other than missing material) should be directed to the corresponding author for the article.

This paper has been typeset from a TEX/LATEX file prepared by the author.